Novel Modulation and Detection Mechanisms in Silicon Nanophotonics

Thesis by

Tom Baehr-Jones

In Partial Fulfillment of the Requirements

for the Degree of

Doctor of Philosophy

California Institute of Technology

Pasadena, California

2006

(Submitted April 20, 2006)

To my parents,

Sonya and Tom

Acknowledgements

I would like to thank Professor Axel Scherer for his guidance and support, and for providing me with the opportunity and resources to complete my Ph.D. Caltech has been a wonderful environment for learning about the scientific world, and developing my own interests. I would like to thank Michael Hochberg, Guangxi Wang, and Chris Walker for helping me with the fabrication and testing component of the devices described in this thesis.

I would also like to thank my parents and entire family for their continued support and help over the years. I will always be greatly indebted to them.

List of Publications

[1] T. Baehr-Jones, M. Hochberg, C. Walker, and A. Scherer, “Analysis of the tuning sensitivity of silicon-on-insulator optical ring resonators,” IEEE J. Lightwave Technology 23, 4215-4221 (2005).

[2] T. Baehr-Jones, M. Hochberg, G. Wang, et al., ”Optical modulation and detection in slotted silicon waveguides,” Optics Express 13, 5216-5226 (2005).

[3] M. Hochberg, T. Baehr-Jones, C. Walker, et al., “Segmented waveguides in thin silicon-on-insulator,” Journal of the Optical Society of America B 22, 1493-1497 (2005).

[4] J. Witzens, T. Baehr-Jones, A. Scherer, “Hybrid superprism with low insertion losses and suppressed cross-talk,” Physical Review E 71, Art. No. 026604 (2005).

[5] T. Baehr-Jones, M. Hochberg, C. Walker, et al., “High-Q optical resonators in silicon-on-insulator based slot waveguides,” Applied Physics Letters 86, Art. No. 081101 (2005).

[6] M. Hochberg, T. Baehr-Jones, C. Walker, et al., “Integrated plasmon and dielectric waveguides,” Optics Express 12, 5481-5486 (2005).

[7] T. Baehr-Jones, M. Hochberg, C. Walker, et al., ”High-Q resonators in thin silicon-on-insulator,” Applied Physics Letters 85, 3346-3347 (2004).

[8] B. Maune, M. Loncar, J. Witzens, et al., “Liquid-crystal tuning of a photonic crystal laser,” Applied Physics Letters 85, 360-362 (2004).

[9] J. Witzens, M. Hochberg, T. Baehr-Jones, et al., "Mode matching interface for efficient coupling of light into planar photonic crystals," Physical Review E 69, Art. No. 046609 (2004).

[10] J. Witzens, T. Baehr-Jones, M. Hochberg, et al., "Photonic crystal waveguide-mode orthogonality conditions and computation of intrinsic waveguide losses," Journal of the Optical Society of America A 20, 1963-1968 (2003).

[11] M. Hochberg, T. Baehr-Jones, G. Wang, et al., "Terahertz all-optical modulation in silicon-polymer hybrid system," *in review.*

[12] M. Hochberg, T. Baehr-Jones, "A method and apparatus for heterogeneous distributed computation," United States Patent Application (2001).

[13] T. Baehr-Jones, M. Hochberg, A. Scherer, "Integrated plasmon and dielectric waveguides," United States Patent Application (2005).

[14] T. Baehr-Jones, M. Hochberg, A. Scherer, "Near field scanning microscope probes and method for fabricating same," United States Patent Application (2005).

[15] T. Baehr-Jones, M. Hochberg, "A computer-implemented method for solving differential equations describing a physical system," United States Patent Application (2005).

[16] T. Baehr-Jones, M. Hochberg, A. Scherer, "Plasmon waveguide light concentrators," United States Patent Application (2005).

[17] T. Baehr-Jones, M. Hochberg, A. Scherer, C. Walker, J. Witzens, "Segmented waveguide structures," United States Patent Application (2005).

[18] T. Baehr-Jones, M. Hochberg, A. Scherer, C. Walker, J. Witzens, "Coupled segmented waveguide structures," United States Patent Application (2005).

[19] M. Hochberg, T. Baehr-Jones, A. Scherer, “Split ring optical cavities and split optical cavities with electrical connections,” United States Patent Application (2005).

[20] M. Hochberg, T. Baehr-Jones, A. Scherer, “Advanced time-multiplexed etching technique,” United States Patent Application (2006).

[21] T. Baehr-Jones, M. Hochberg, “A novel geometry for the detection of optical radiation,” United States Patent Application (2005).

[22] M. Hochberg, T. Baehr-Jones, “Bremstrahlung laser (BLASER),” United States Patent Application (2005).

[23] M. Hochberg, T. Baehr-Jones, “Quantum dot composite laser,” United States Patent Application (2005).

[24] M. Hochberg, T. Baehr-Jones, A. Scherer, “ICP PECVD deposited layers as a protective cladding for polymer-based devices,” United States Patent Application (2005).

[25] M. Hochberg, T. Baehr-Jones, “Frequency conversion with nonlinear optical polymers and high index contrast waveguides,” United States Patent Application (2005).

[26] M. Hochberg, T. Baehr-Jones, “Ultrafast optical modulator,” United States Patent Application (2005).

Abstract

A number of nanophotonic integrated circuits are presented, which take advantage of the unique properties that light has when guided in very small waveguides to achieve novel functionality. The devices studied are designed to operate with light in the 1400-1600 nm range.

Nanophotonic integrated circuits are tiny waveguides and other optical devices that are fabricated on the nanometer (10^{-9} meter) scale. These waveguides are often two orders of magnitude smaller than more conventional optical waveguides, such as a fiber optical cable. This reduction in size is interesting because it opens the possibility that expensive optical components might be integrated in very small areas on a chip, and also because the concentrated fields that result from this compression can be used to produce new optical functionality.

First, the techniques used to design passive optical structures, and the methods used to test them, are discussed. Most of the waveguides studied are fabricated from 110 nm thick layers of silicon from silicon-on-insulator wafers. The best waveguide loss achieved was -2.8 dB/cm. Also described are waveguides based on utilizing surface plasmon waves to guide light.

The use of second order nonlinear optical polymers for modulation is also discussed. These polymers are integrated into Silicon slot waveguides, where the Silicon itself serves as the electrode. Modulation is achieved via the Pockels effect. The

modulation figure of merit obtained for the device is superior to the contemporary state of the art, an improvement due to the nanoscale nature of the waveguide. Additionally, detectors based on these same polymers and waveguide geometry are presented. Though the detection efficiency is not very high, the detectors are interesting because they do not require any external power supply, and because they have virtually no speed ceiling.

Finally, the use of third order nonlinear optical polymers for all-optical modulation is discussed. When integrated with ridge waveguides, such polymers enable all-optical modulation. Several experiments are described that demonstrate that all-optical modulation has been achieved.

Contents

List of Figures

It must be noted that in all of what follows, simulation rarely matched the observed results exactly. This is due to the fact that things such as the wafer thickness, and the exact locations of the etch are not exactly aligned with the same values used in the simulation. Thus, one cannot expect values such as the effective index to be exact.

Glossary of Acronyms

E Electric Field

H Displacement Magnetic Field

FDTD Finite-Difference Time Domain

Q Quality Factor

PMMA Polymethylmethacrylate

SOI Silicon-On-Insulator

DC Direct Current

RF Radio Frequency

dB Decibel

V Volt

pm Picometer (10^{-12} m)

Chapter 1

Introduction

The past twenty years have seen an incredible development of the field of fiber optics, and more generally, optics in the telecommunication near infrared regime (1000-1600 nm free space wavelength) [1]. One can currently obtain an erbium-doped fiber amplifier (EDFA) as a piece of standard communications equipment, which is capable of outputting nearly 1 Watt of laser power [2]. Highly sensitive detectors, easily controlled tunable lasers, and high quality fiber connectors are all cheaply and easily available. It would not be much of an exaggeration to say that the modern telecommunications optics engineer has a great deal more at his disposal than any of his predecessors. This growth in capability is due mainly to the incredible demand for bandwidth created by the development of the Internet.

Great increases in capability can also be found, of course, in the semiconductor manufacturing field. The exponentially more powerful CPU, and the ever increasing market demand that they have been met with, has made the fabrication of very small, very pure silicon structures one of the most accurate tasks achievable with modern means.

These two seemingly distinct fields have an important overlap in the so-called field of nanophotonics. It is widely known that many common semiconductor materials, including Silicon, are transparent to radiation in the near infrared regime [3]. One can

form waveguides to guide this radiation, in various configurations. As this thesis will show, one such configuration is a simple ridge of dimensions 500x110 nm [4]. Though this is about 10^{-4} of the effective area of a fiber mode, relatively low loss guiding can still be observed.

There are several exciting possibilities in the field of nanophotonics. The first is the elimination of the conventional bulk photonics components currently in use in industry, and the vast integration of these materials into single chips; this would be a transition not unlike that by which conventional vacuum tube based electronics were eventually replaced by the integrated circuit.

There is reason to believe that it may soon be practical to implement most of the photonics devices involved in modern telecom entirely on a chip. In fact, Luxtera Inc., founded in 2001, is currently trying to perform such an implementation in Silicon [5]. It remains to be seen if this effort will meet with commercial success, though it seems likely that it will.

The benefits of such a transition are obvious. One imagines the current pieces of bulky equipment at the end of fiber optical components with compact computer chips. The savings in space and cost with such an approach may even result in new high bandwidth consumer products. The work I have done in the past three years does bear application to such areas, but that is not what my main focus has been.

I believe that there is a second opportunity presented by nanophotonics-the possibility of low power nonlinear behavior. This is due to the fact that, by virtue of simply having smaller transverse dimensions, nanophotonic waveguides have relatively

large electric fields for a given amount of power, when compared to more conventional waveguides. For example, a fiber optical waveguide as found in typical fiber optics cables has a modal electric field of nearly 1/100th the strength of the electric field in the ridge waveguide mode, for a given amount of steady state power. When this fact is combined with the capability to obtain resonator Q's in excess of 70,000, it is not unreasonable to expect that field enhancements due solely to the geometry in the regime of 10^4 times may be obtained. In the various devices described in this work, field magnification values of 10^3 times are already routinely obtained. It is especially interesting to consider the effect this has on things such as the Kerr effect, which involves the square of the electric field. In this case, nearly eight orders of magnitude increase in the effect might be achieved by virtue of the new abilities conferred by nanophotonics.

The feasibility of making nonlinear optical devices, especially for computation, has long been hindered by the monumental powers required for any non-negligible nonlinear effect to be observed. It is my belief, however, that this limitation will be shattered in the near future, by means of the massive field enhancements conferred through nanophotonics waveguides.

This thesis will discuss my work over the past three years, which is partially devoted to the development of passive nanophotonics, and partially devoted to the use of such passive photonics to enhance nonlinear effects. In chapter 2, I will discuss the basic tools of electromagnetic modeling that were used for the design of the structures studied. Because of the high index contrast-the optical index of the waveguide core, Silicon, is 3.4, while the index of the cladding is only 1.7 or less, and the waveguide dimensions are of the same order of magnitude of the wavelength-design is challenging. Many of the

conventional approximations used for optics break down, and nearly exact simulation methods are thus needed. I say nearly exact, as the only error is due to the discretization of Maxwell's equations, and in the limit that the discretization were to tend to 0, an exact result would be obtained.

I will then discuss work I have done in relation to the design of Silicon ridge waveguides in chapter 3, and I will talk about some of the basic problems that must be solved in order to make passive integrated optics systems viable. Chapter 4 discusses using metals to guide light via surface plasmon waveguides. I will show that with plasmon waveguides, light can be compressed down into an extremely small modal volume, with relatively little insertion loss from a Silicon waveguide.

Chapter 5 discusses the use of nanophotonic waveguides to enhance the performance of modulators. I will show, also, that the use of Silicon as a waveguide has significant benefits, allowing both the waveguide and a contact to be made of the same material. Chapter 6 shows that this same configuration actually allows optical detection, because of the extraordinary concentration of the optical field across an electrode gap. Finally, in Chapter 7 I discuss the use of the field concentrations intrinsic in our waveguides to achieve all optical modulation, at relatively low power.

Taken together, I believe the results obtained do bear out what my aim was in this work – to show that nanophotonic waveguides have the potential to provide completely new classes of functionality, based on their intrinsic abilities to concentrate field. Only time will tell whether we will someday see optical computation devices or other practical engineering based on these principles, but I believe important strides towards this possibility are described in this work.

Chapter 2

Electromagnetic modeling

2.1 Maxwell's equations

Computational modeling of Maxwell's equations is critical for work in integrated optics, as well as in a number of other fields. These include antenna design, radar cross section prediction, electronics design, and many others. A key enabler for the optical devices we have developed is the ability to accurately predict the behavior of the finished structures. Prior to beginning my graduate work at Caltech, I developed the first commercial distributed Finite-Difference Time Domain electrodynamics code [6]. This code was used extensively throughout the design of the optical devices described within this thesis, and will be extensively described in this chapter.

The fundamental problem in electrodynamics is the solution to the linear, 6-vector Maxwell's Equations [7]. In general, analytical solutions to these equations are not available for problems beyond the very simplest cases. As a result, there has been extensive work over the past 50 years on developing methods to solve them computationally. Many techniques rely on some simplification of the problem – in the various physical limits, there are a variety of sensible simplifications that can be made. For instance, where the wavelength of interest is large compared to the domain of interest, one can solve Poisson's equation, which is computationally much simpler than the full 6-vector Maxwell's equations. In the limit where the wavelength is much smaller

than the structures, it is often possible to use bouncing-ray, ray-tracing, or physical-optics approximations [8]. Although such methods can significantly improve the speed with which solutions can be obtained, they all fail when the problem is not in the relevant physical limit.

For the problems of integrated optics, it is not possible to discard any of the physics of Maxwell's equations; the full 6-vector system must be solved. For our integrated optical structures, the devices are on the same order of size as the wavelength of the light. Because they integrate sub-wavelength scattering elements, it is critical to be able to model the response of the structures with the highest possible accuracy. Our devices require solutions to Maxwell's equations in the hyperbolic limit; there are usually order unity wavelengths on the scale of the structural features.

2.2 Survey of current computational methods

There are two widely used approaches to solving such problems: FDTD [9], and finite element techniques [10]. Finite element techniques are based upon a decomposition of a 3-D domain into tetrahedral elements, which have Maxwell's equations projected onto them and discretized. A linear system is then solved, which provides an estimate to the true, continuous solution. The process of solving a very large linear system, however, is extremely taxing computationally, leading to limitations on the scale of problems that can be addressed with this method. The most important limitation is that at least parts of the entire matrix must be stored in memory; generally speaking, if these parts are larger than the available memory, the simulation will either crash or slow down by orders of

magnitude, rendering such simulations impractical. The most popular finite element software is frequency-domain, and yields steady-state solutions to Maxwell's Equations as a function of frequency [11].

Finite Difference Time Domain is a method which has gained substantial acceptance over the last two decades for simulating problem domains that are too large to handle in finite element techniques. FDTD is an explicit technique, and gives solutions in the time domain. Because FDTD uses a uniform mesh, the memory overhead per point is much smaller – the locations of each grid point do not have to be stored. Although this means that more points often have to be used in order to represent smooth or curved structures accurately, the reduction in memory overhead per point means that dramatically more points can be stored in the same memory space.

On a PC with 2 gigabytes of RAM, it is not unusual for many finite element implementations to limit out at about 400k tetrahedra. By contrast, a 2 GB FDTD domain can support nearly 90 million FDTD pixels, which are roughly comparable in computational utility to a finite element tetrahedron, at least for the purposes of a hyperbolic equation. This is because both FDTD and finite element are based on a Taylor expansion of Maxwell's equations to second order accuracy. Such an expansion is limited mainly by the maximum difference between sampling points, or more plainly, the number of sampling points per wavelength. Any local benefits accrued from marginally more sophisticated finite elements are vastly outweighed in the hyperbolic limit by simply minimizing the radial parameter to the Taylor expansion. Hence, FDTD is usually a superior method, at least for large domains.

As mentioned in the introduction, the FDTD implementation used was one that I wrote about 5 years ago, prior to my graduate work at Caltech. Crucially, this implementation had the ability to run on multiple PCs at the same time, which greatly raises the sizes of domains that can be used for simulations [6].

2.3 Modal analysis

Before discussing the specifics of using FDTD for optical device simulation, an even more important question must be answered. The first step in the analysis of any nanophotonic optical device is of course an analysis of the modal profile of the guided modes in the waveguide structure. Indeed, a study of the precise optical properties of the waveguides to be used is usually the first step in choosing a material system to work in, and is the first constraint upon device design.

The usual mathematical problem is phrased as follows: given a continuous symmetry in the z direction, find the E, H distributions, as well as the propagation constant and corresponding frequencies, for which Maxwell's equations are satisfied. Taking our structure to be defined as $\varepsilon(x,y)$, this can be phrased as the generalized eigenvalue equation [12]

$$H\Psi = i\beta A\Psi$$

where

$$H = \begin{pmatrix} iw\varepsilon_0\varepsilon(x,y) & 0 & 0 & 0 & 0 & \partial_y \\ 0 & iw\varepsilon_0\varepsilon(x,y) & 0 & 0 & 0 & -\partial_x \\ 0 & 0 & iw\varepsilon_0\varepsilon(x,y) & -\partial_y & \partial_x & 0 \\ 0 & 0 & -\partial_y & iw\mu_0 & 0 & 0 \\ 0 & 0 & \partial_x & 0 & iw\mu_0 & 0 \\ \partial_y & -\partial_x & 0 & 0 & 0 & iw\mu_0 \end{pmatrix}$$

$$A = \begin{pmatrix} 0 & 0 & 0 & 0 & 1 & 0 \\ 0 & 0 & 0 & -1 & 0 & 0 \\ 0 & 0 & 0 & 0 & 0 & 0 \\ 0 & -1 & 0 & 0 & 0 & 0 \\ 1 & 0 & 0 & 0 & 0 & 0 \\ 0 & 0 & 0 & 0 & 0 & 0 \end{pmatrix}$$

Another, more useful way of phrasing the problem is as follows [13]:

$$\nabla \times \frac{1}{n(r)^2} \nabla \times H = \frac{w^2}{c^2} H$$

Here w^2 is the eigenvalue to be deduced. The propagation constant β is a parameter to the problem. In an ideal world, one would like to select what is always known in advance, the w of interest, and thus derive the β and modal pattern. However, proceeding in the other direction is not too much trouble. Of course, we are still left with the nontrivial problem of solving a large Hermetian eigenvalue problem. This is done by a technique I have developed that is similar to the Rayleigh quotient iteration, and which is detailed elsewhere [14].

2.4 Standard simulation techniques

Between the ability to solve for guided modes and the capability to evolve solutions forward in time with FDTD, only a few additional features are required for complete simulations. First, one must be able to launch perfectly guided modes. A typical simulation may be the derivation of the coupling constant between two neighboring

waveguides. What one really wants in such a situation is the steady state propagation pattern between the various ports. This can be obtained by firing a wavepacket composed of the appropriate guided mode down one of the waveguides, and taking a Fourier transform at each desired port surface. A typical screenshot from an FDTD simulation is shown in figure 2.1.

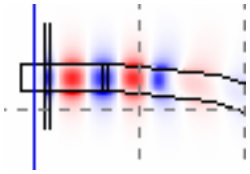

Figure 2.1: In FDTD, a wavepacket composed of the guided mode prorogating down a waveguide.

A guided mode as shown in Figure 1 can be launched by first projecting the FDTD differential equations into the frequency domain. The guided mode will be a solution to these, if the mode is extended in the third dimension with the proper β, with 0 associated current. If the mode is truncated at an artificial wall, however, and the Maxwell equations are applied, a current pattern will be found, which can be projected back into the time domain with a Fourier transform. When used as an FDTD current source, this results in the mode being launched.

It should be noted how a true modal amplitude can be extracted from a steady-state field pattern, which does not necessarily contain solely the guided mode. Through the use of the generalized eigenvalue equation form of Maxwell's equations in the guided mode problem, one can define an inner product, if ψ is taken to be the full E, H 6 vector, as [15]:

$$(\psi_a, \psi_b) = \begin{pmatrix} E_a & H_a \end{pmatrix}^t A \begin{pmatrix} E_b \\ H_b \end{pmatrix}$$

$$A = \begin{pmatrix} 0 & 0 & 0 & 0 & 1 & 0 \\ 0 & 0 & 0 & -1 & 0 & 0 \\ 0 & 0 & 0 & 0 & 0 & 0 \\ 0 & -1 & 0 & 0 & 0 & 0 \\ 1 & 0 & 0 & 0 & 0 & 0 \\ 0 & 0 & 0 & 0 & 0 & 0 \end{pmatrix}$$

Though this is not a proper norm, it has several useful properties. First, the value (ψ,ψ) is proportional to the classic time averaged Poynting vector. Secondly, modes with differing β values, including the reverse propagating mode, are orthogonal. This norm, along with the mode launch ability described above, is the basis for nearly all quantitative values extracted from the simulations in this work. As an example, a directional coupler shown in Figure 2.2 is characterized by a wavepacket being fired from one of the ports. The wavepacket travels down the waveguide, and is measured while passing past each surface. In such a manner, the coupling coefficients at multiple frequencies are extracted.

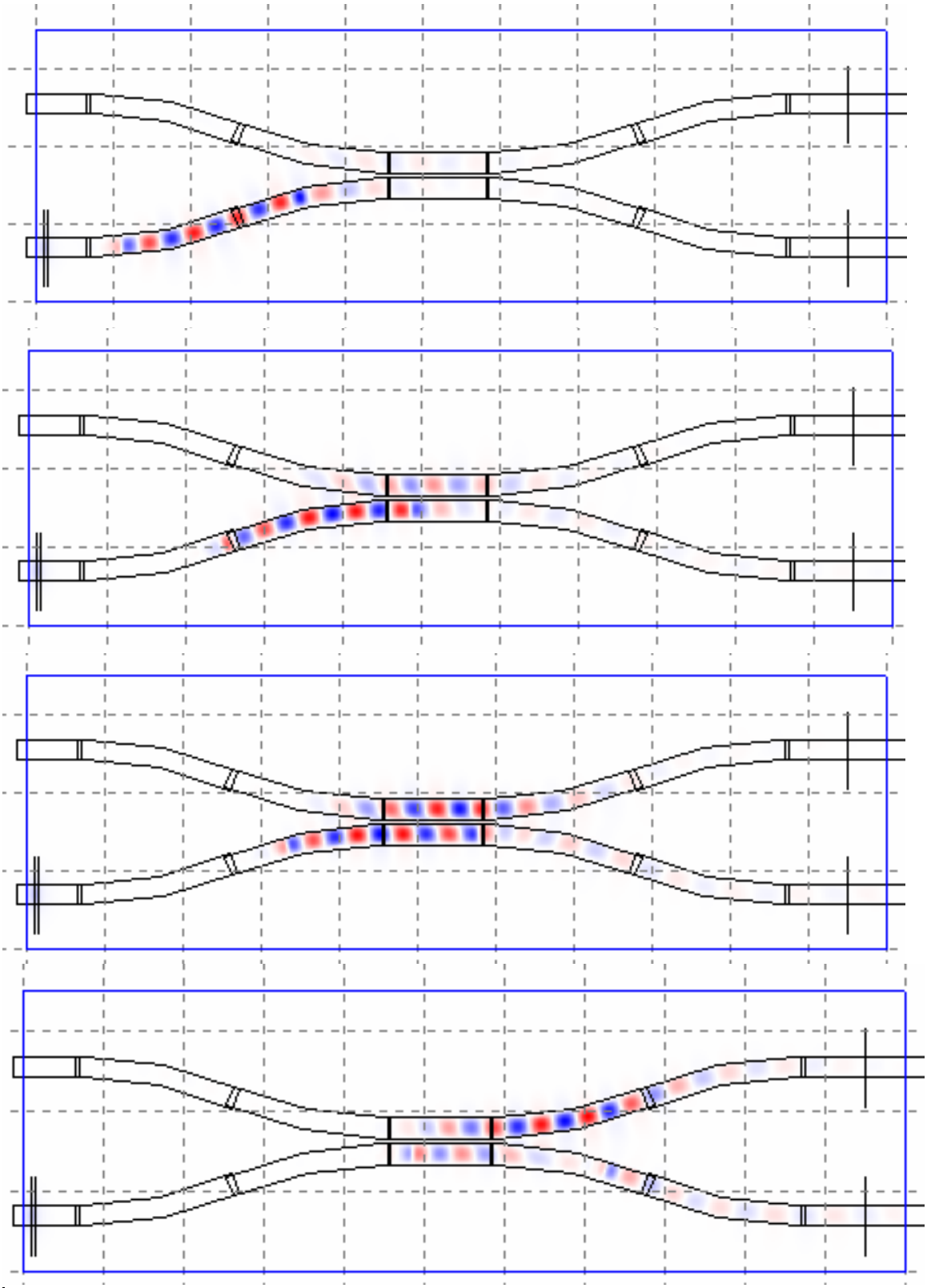

Figure 2.2: Three-dimensional FDTD simulations of a directional coupler at various simulation times. The H component is plotted in the vertical direction, along a plane that bisects the waveguide vertically. This is the primary direction of H polarization for the optical mode, orthogonal to the horizontal E polarization. Note the relatively large bend radii used in the construction of the coupling region. This is due to the previously mentioned large bend radius needed. Such simulations may take on the order of 6 hours on four PC caliber machines.

Chapter 3

Passive Optical Components

3.1 Selection of Material System

The most basic question to answer in working on nanophotonics is which material system to work in. For the work described in this thesis, silicon was selected. Silicon has the drawback of being optically passive, but is easy to work with, and is readily commercially available. It also has fairly low intrinsic optical loss, at least when it is not doped [3].

Most of the electronics industry works in bulk silicon; that is, a wafer of Si that may be hundreds of microns thick has electronic structures patterned on the very top layer [16]. It is difficult to make an integrated optical waveguide from such a substance. One can define lateral bounds with an etch step, but there is still the vast portion of the wafer beneath the surface, which will prevent a guided mode from being formed. One solution is to used Silicon-On-Insulator, or SOI, which is used in commercial electronics for low power applications [17]. Here, a waveguide can be formed with a single step of patterning and etching.

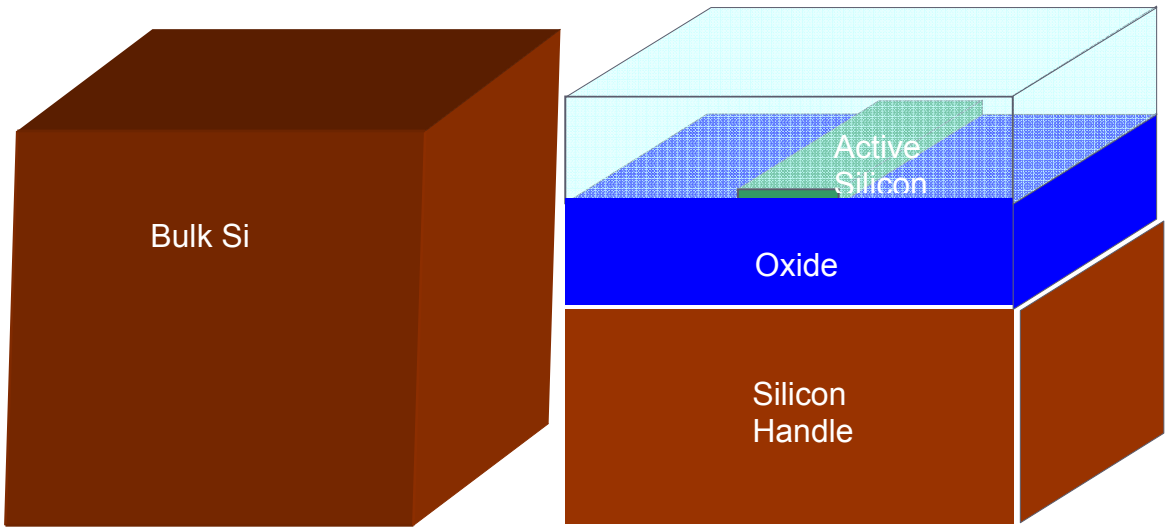

Figure 3.1: Typical wafer cross section of bulk Silicon, left, and Silicon-On-Insulator (SOI), right. The SOI cross section has a ridge waveguide illustrated.

3.2 Ridge waveguide design

If a layer of approximately 110 nm Silicon is etched to produce a 0.5 um wide ridge, a single optical mode will be supported. It will be polarized with the electric field primarily in the horizontal direction [4]. A typical dispersion plot of such a mode is shown in Figure 3.2, as well the field distribution.

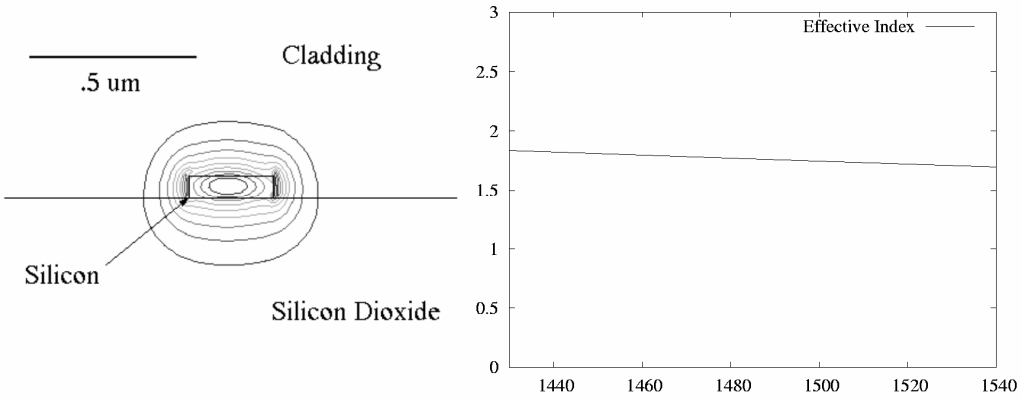

Figure 3.2: Modal profile of the Silicon waveguide and the dispersion plot, as a function of wavelength in nm. The profile is of |E|, with contour lines drawn in increments of 10% starting at 10% of the maximum field value.

Several advantages and disadvantages of this particular waveguide should be noted here. First, the mode is supported with a cladding layer of anything from a refractive index of 1 to a refractive index of 1.7. Also, nearly one-third of the mode's energy is distributed in the upper cladding layer. This means that if the cladding has an optical property modified, then the effect on the optical mode will be more pronounced, compared to a mode that resides nearly entirely inside the Silicon. This makes this kind of waveguide well-suited to some of the experiments that we wished to perform, which involve active materials in the cladding layer.

There are some significant disadvantages that should be noted here, as well. First, because the mode does have a substantial overlap with the cladding layer, it has an effective index that is fairly low, typically only 0.1 above that of the cladding; that is, in a cladding of n=1.7, the mode might have an effective index of 1.8 near a free space

wavelength of 1.55 um. Because of this, there is a substantial amount of bend loss that is exhibited by the mode at even fairly large bend radii. Through the use of ring resonators, a technique to be described later in this work, it was found that substantial bend loss began at about 30 um of radius and less. This is a substantial problem for the construction of truly nanoscale devices, and is also a far worse level of performance than that exhibited by thicker Silicon waveguides [18].

Another problem with this type of mode is that the non-trivial amount of overlap with the cladding results in a heightened sensitivity to surface roughness. That is, small imperfections in the fabrication of the waveguide edge can lead to larger levels of loss with this type of mode than other types of waveguides.

Let us discuss briefly, however, the ultimate relevance of the figure of waveguide loss. In the long run, unless one is able to somehow obtain gain, there is no question that minimizing loss is a key to making such systems practical. But how much minimization is necessary? It depends on the application. In conventional telecom applications, perhaps the two biggest pieces of functionality involve modulation, and mux/demux devices. In both cases, basic physical necessities require an amount of path length in the device to accomplish these tasks, which turns out in both cases to be on the order of a centimeter. Acceptable levels of loss for bulk components tend to be on the order of 5-7 dB [19]. As a result, nanophotonics waveguides will become competitive, for lack of a better term, in the sub 3 dB/cm regime. Since this level of loss was obtained, as will be discussed later in this chapter, even with these waveguide designs, and even in a university setting, it is not clear to me that the issue of loss is still a governing consideration in the choice of waveguides as it once was.

There is one more consideration that should be mentioned. This is the peak electric field exhibited in a guided optical mode in this type of waveguide. 1 milliwatt of optical power propagating in this ridge waveguide produces a peak field intensity, which occurs at the lateral edges of the waveguide in the cladding region, of about $3x10^6$ V/m. For comparison, 1 milliwatt propagating in a conventional single mode fiber produces an approximate peak E field of $3x10^4$ V/m. The benefits of a nanoscale waveguide are apparent.

3.3 Fabrication techniques

Michael Hochberg was primarily responsible for the fabrication of these devices. Briefly, the fabrication procedure can be described as follows: SOI material with a top silicon layer of approximately 110 nm and 1.35 micron bottom oxide was obtained in the form of 200 mm wafers, which were manually cleaved, and dehydrated for 5 minutes at 180^{o}C. The wafers were then cleaned with a spin/rinse process in acetone and ispropanol, and air dried. HSQ resin electron beam resist from Dow Corning Corporation was spin-coated at 1000 rpm and baked for 4 minutes at 180^{o}C. The coated samples were exposed with a Leica EBPG-5000+ electron beam writer at 100 kV. The results reported here are for devices exposed at a dose of 4000 microcoulombs/cm^2, and the samples were developed in MIF-300 TMAH developer and rinsed with water and isopropanol. The patterned SOI devices were subsequently etched by using an Oxford Plasmalab 100 ICP-RIE within 12 mTorr of Chlorine, with 800 W of ICP power and 50 W of forward power applied for 33 seconds. Subsequently the devices were spin-coated with 11% 950K PMMA in Anisole, at 2000 rpm, and baked for 20 minutes at 180^{o}C [4].

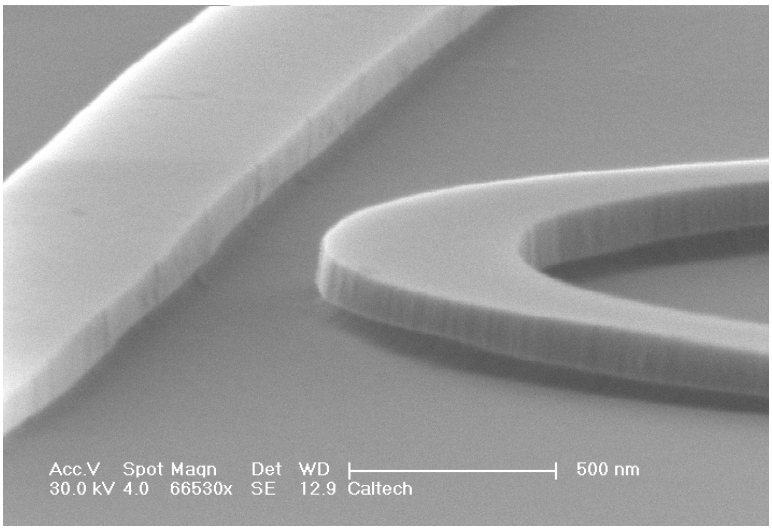

Figure 3.3: SEM image of ridge waveguide. Here it is part of a ring resonator device.

It must be noted that in all of what follows, simulation rarely matched the observed results exactly. This is due to the fact that things such as the wafer thickness, and the exact locations of the etch are not exactly aligned with the same values used in the simulation. Thus, one cannot expect values such as the effective index to be exact. Instead, a trend in device behavior must be identified, and then the precise values needed to match the exact behavior needed discovered in a series of empirical studies.

3.4 Input coupling and passive testing procedures

Of course, the most basic question one might have upon hearing this description of the waveguide might be how it can be conveniently coupled into. As it stands, the mode has a cross section of approximately 0.5x0.11 um, which is far smaller than what might be found in a fiber mode, where the mode falls in a circle of diameter about 20 um. Though

it is possible to butt-couple a fiber mode directly to a ridge waveguide, it is only by squeezing the ridge waveguide until the mode becomes quite large [20]. Any butt-coupling method will also induce difficulties in testing, as the fiber must be aligned from the side of the chip.

A superior way of performing this coupling is through the use of a grating coupler. These devices first flare out in a plane to expand the ridge mode into a large, slab mode, and then consist of a series of scattering sites that scatter the mode into a larger angle. When designed properly, reasonable efficiencies can be obtained [21]. We employed such a methodology here, achieving -6 dB insertion losses with about 40 nm of bandwidth.

The advantage of this method is that, first, the input couplers can be defined in a limited, isolated area of the chip. Waveguides can circle entirely around the coupler. Secondly, large scale automated test can be performed through the use of a computer controlled fiber array. Through this method, literally thousands of devices can be aligned and tested.

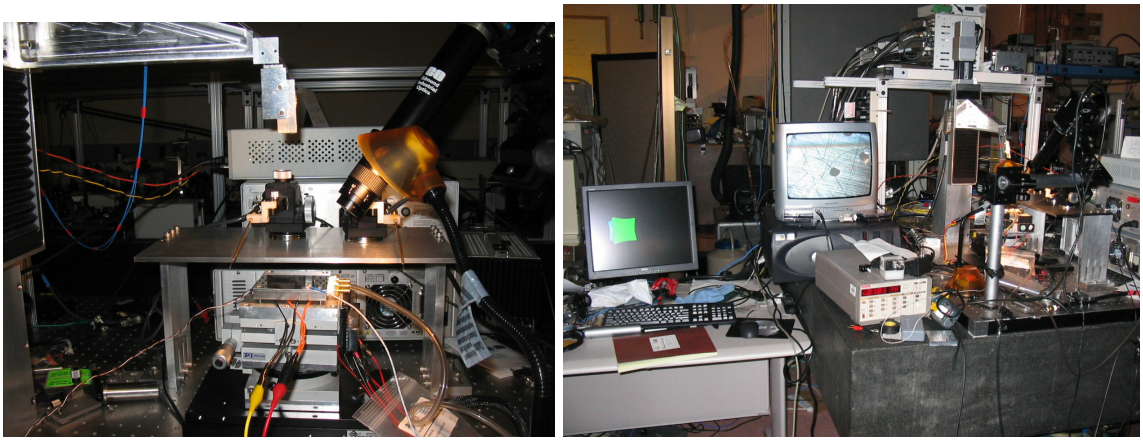

Figure 3.4: Image of computer controlled test setup, which uses a fiber array to vertically couple into the chip.

Typical testing methodology for passive devices consisted of measuring the transmission through a device as a function of frequency. When combined with the ability to test many devices, a clear picture of the performance of a class of components could be obtained.

3.5 High Q ring resonators

The most basic characteristic to obtain about a given waveguide, beyond simply whether or not it transmitted light from grating coupler to grating coupler, was what the loss was. One method of deriving this loss was to write very long waveguide structures, and perform a linear regression on the transmission versus the length. However, this suffers from the problem that macroscopic defects may cause excess loss, such as boundaries between fields in the electron-beam writer. While this can be argued to be legitimate loss, what is more interesting is the loss from small, localized devices. This is best deduced via the construction of ring resonators, and the measurement of their Q factors. The

waveguide loss can be calculated from this. Such structures are also interesting because they have applications for mux/demux, as well as detection and modulation.

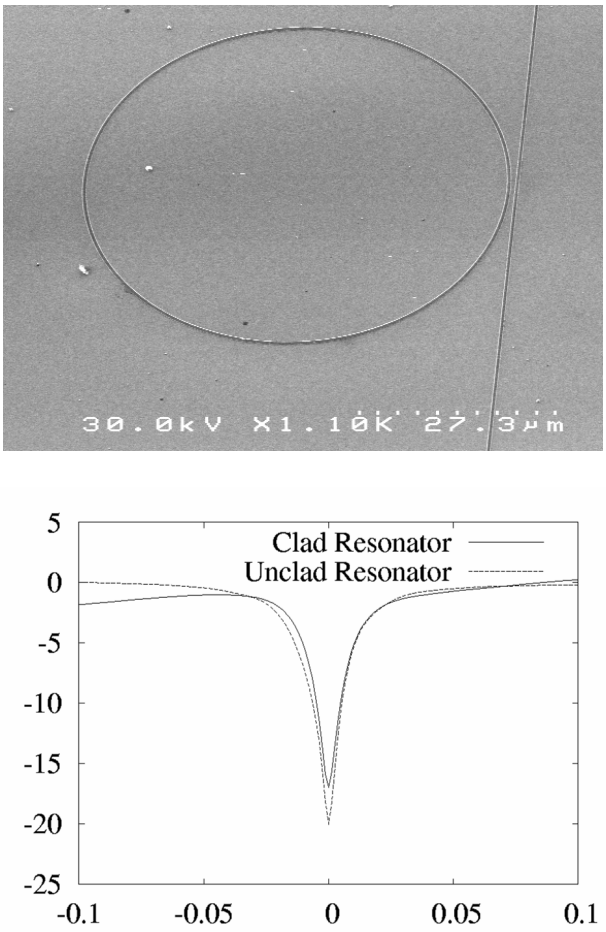

Figure 3.5: SEM image of ring resonator, and plot of transmission past device. The high Q resonance peaks are clearly visible. Also shown is the transmission spectrum past the resonator, normalized to remove coupling losses from the grating coupler and the test setup. Both a PMMA clad resonator and an unclad resonator are shown.

The basic characteristics of a ring resonator used to relate parameters such as waveguide loss to the observed transmission spectra have been described elsewhere [22]. However, a

crucial point must be noted here. In this case the dispersion of the waveguide compels the addition of a dispersive term to the peak width. We take λ_0 to be the free space wavelength of a resonance frequency of the system, n_0 to be the index of refraction at this wavelength, $(\partial n/\partial\lambda)_0$, the derivative of n with respect to λ taken at λ_0, L the optical path length around the ring, α the optical amplitude attenuation factor due to loss in a single trip around the ring, and finally t the optical amplitude attenuation factor due to traveling past the coupling region. In the limit of a high Q, and thus $(1-\alpha)<<1$ and $(1-t)<<1$, we have

$$Q=\frac{\pi L}{\lambda_0}\frac{\left(n_0-\lambda_0\left(\frac{\partial n}{\partial\lambda}\right)_0\right)}{(1-\alpha t)}$$

The intrinsic Q of such a ring, that is, the Q one would observe in the absence of any waveguide coupling, can be calculated by simply taking the limit of the previous formula as t goes to 1. Then, we have

$$Q_i=\frac{\pi L}{\lambda_0}\frac{\left(n_0-\lambda_0\left(\frac{\partial n}{\partial\lambda}\right)_0\right)}{(1-\alpha)}$$

The waveguide mode was coupled into a ring resonator from an adjacent waveguide. The strength of coupling can then be lithographically controlled by adjusting the distance between the waveguide and the ring.

3.6 Waveguide loss analysis

Our initial waveguide designs were found to have an approximate loss value of -7 dB/cm. This is already a fairly high value – Q values in excess of 50k were detected. To see what the limit on waveguide loss would be, it is appropriate to consider the possible sources of loss. First, there are material losses intrinsic to Silicon. These include two-photon absorption and surface recombination. We have found, also, that these losses rise as the Silicon is doped. Work from Painter et al [18] suggests that this may be less than .1 dB/cm for intrinsic Silicon.

Another source of loss is surface roughness. We initially suspected that much of the 7 dB/cm figure was due to this. However, a third possibility was the effect known as substrate leakage. Essentially, this is due to the fact that the SiO_2 substrate layer beneath the top Silicon layer does not go down forever, but in fact terminates in a bulk Silicon handle. This handle then drains energy from the optical mode. The precise loss can be predicted via perturbation theory, and was predicted to be approximately -3.5 dB/cm for the 1.35 um substrate. In later work, a substrate of depth 3 um was used, and loss was found to drop to about -2.8 dB/cm, confirming this prediction. The further decrease is probably due to other changes in technique, such as better etching.

As one would expect, with the lower waveguide loss, the Q values of the ring resonators were correspondingly higher. In fact, Q values of over 160 k were obtained.

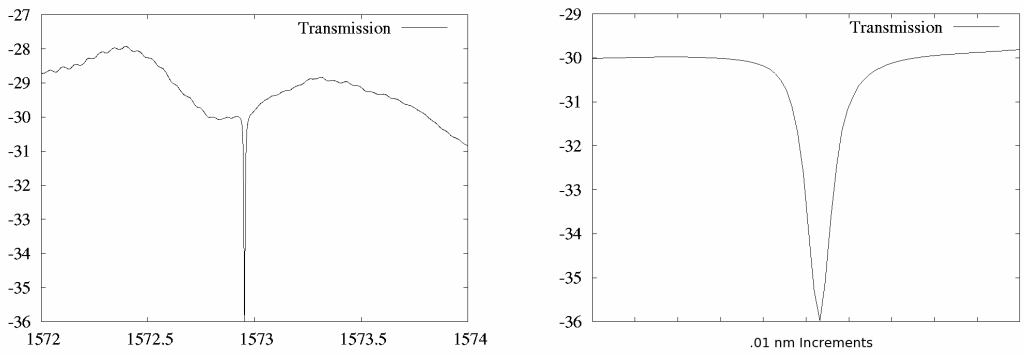

Figure 3.6: Transmission spectrum of a particularly high Q ring resonator. The Q is in excess of 160 k.

3.7 Monolayer electrical contacts with segmented waveguides

One of the benefits of using Silicon, as opposed to silicon dioxide, for a guiding structure, is that electrical contact can be made directly through the Silicon. Of course, some doping is generally required to achieve acceptable conductivities for most applications [16], and as mentioned before this causes the waveguide loss to increase. However, in practice there is a happy medium, in which doping-induced optical losses are still less than 1 dB/cm, but the Silicon is sufficiently conductive. This will be discussed at greater length in the section describing modulation.

Of course, to use this fact, one needs to form some sort of electrical contact with the waveguide in the first place, and preferably close to the region where the optical activity is occurring. However, the definition of an electrical contact on such a waveguide is particularly difficult since the waveguide is both electrically and optically isolated on all sides by silicon dioxide cladding. The introduction of most arbitrary electrical contacts would lead to a significant interruption in the waveguide symmetry, and therefore a large

scattering loss. Here we show a remedy for this problem by constructing segmented waveguides as shown in Figure 3.7.

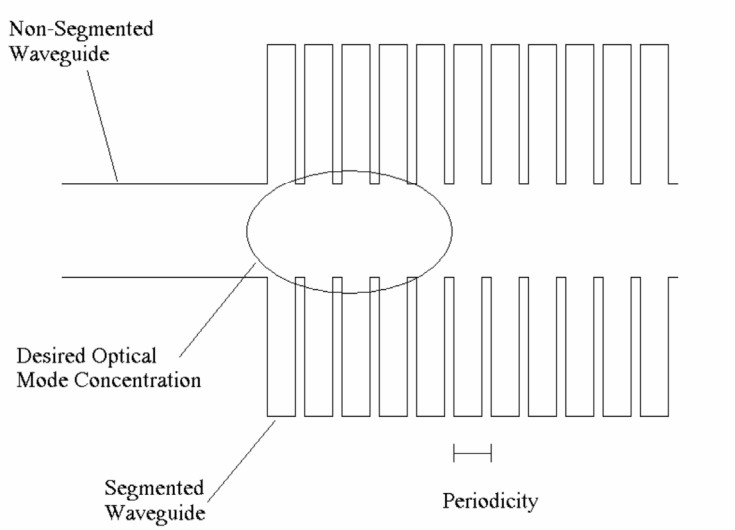

Figure 3.7: Logical diagram of the design of a segmented waveguide.

The electrical contact is defined as a lateral "grating" or a planar extension that is lithographically defined during the same lithographic step as the waveguide definition etch. The optical properties of this geometry are strongly dependent on the periodicity and duty cycle (We consider duty cycle to be the fraction of the period that contains the segment; thus a duty cycle of .7 on a period of 1 um indicates segments of Silicon that are .7 um long). In theory, the lateral Silicon strips in Figure 3.7 continue forever, but as we will see, for properly chosen periodicities these can be terminated after a relatively short isolation distance. If a low loss, propagating optical mode exists for a particular design, it is possible to achieve both the desired low loss optical guiding as well as lateral electrical contacts to the waveguide [23].

The basic paradigm for waveguide analysis described previously, that is, the removal of the direction of symmetry and the solution of the Hermetian eigenvalue equation, is fully applicable here. The single substantial difference is the replacement of continuous symmetry with discrete symmetry. For the proper periodicity and duty cycle, the existence of contained, well-guided modes is predicted. In the case of the waveguide geometry previously described, an acceptable periodicity turns out to be 0.28 um, and the duty cycle .5. In fact, -16 dB/cm was achieved with this design; while this is enough loss to be a substantial limiting factor for long devices, for short contact regions this is an entirely acceptable level of loss. This is especially true given that the insertion loss due to a straight transition from a normal to segmented waveguide in this configuration is less than .2 dB.

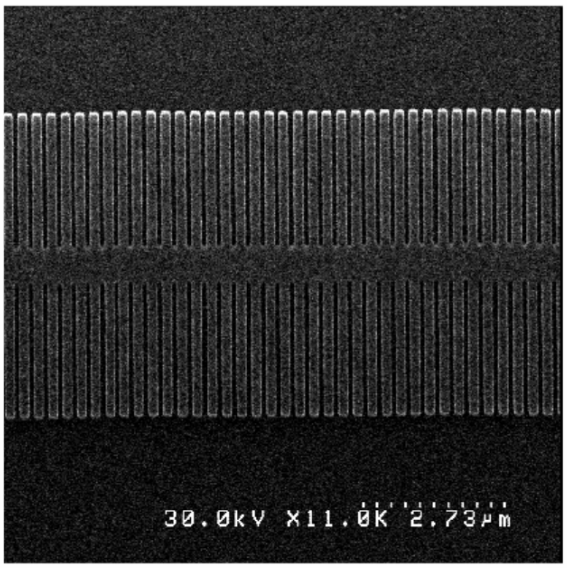

Figure 3.8: SEM image of fabricated segmented waveguide.

Chapter 4

Plasmon Waveguides

4.1 Motivation for guiding with plasmons

Plasmons are waves formed by oscillations of charge in metals [24]. In practice, what this amounts to is that for optical frequencies, below the Plasmon resonance frequency, which for most metals lies in the 400-800 nm range, the interaction of electromagnetic radiation with metals is best described by a largely imaginary index of refraction, which moreover has a magnitude often on the order of 10. In other words, the characteristic wavelength of radiation for a given frequency drops by an order of magnitude in metal. Another interesting effect that this creates is the possibility of guided modes that exist solely on the surface of metals, or surface plasmon waves.

One of the goals of our work in lab, and of nanophotonics in general, is to enable new functionality based on optical nonlinearities that are experienced by light propagating in very small waveguides. There is, however, an ultimate limit to the lateral dimensions of a dielectric waveguide thus formed, the diffraction limit of light. That is, one cannot build a waveguide with lateral dimensions much less than the wavelength of the radiation to be guided divided by the refractive index of the guiding material. For example, if the ridge waveguide described in this work is made narrower, the optical mode will in fact begin to expand, ultimately becoming arbitrarily large. In the context of

a struggle to minimize mode size, then, it is clear that the existence of materials with large refractive indices is interesting.

4.2 Design and fabrication of plasmon waveguides

There is a basic trade-off in all plasmon waveguide geometries between mode size and propagation loss. One can have a low propagation loss at the expense of a large mode size, such as in the work of Nikolajsen et al., who report propagation losses of 6 dB/cm for 20 nm slabs of gold, but with a 12 μm mode diameter [25]. At the other extreme, Takahara et al have predicted guiding in 20 nm diameter silver nanowires, with a mode field diameter of about 10 nm, but with theoretical propagation losses of 3 dB/410 nm [26]. Though this loss is acceptable for nanoscale photonic circuitry, large scale integration with such losses is not feasible.

The aforementioned FDTD implementation was used to design plasmon waveguides by implementing the Drude model to simulate the interaction of the optical field with the metal [27]. A spatial discretization of 10 nm was used, with a time discretization 90% of the stability limit [9]. The modes of a plasmon waveguide formed on the edge of a 100 nm thick layer of silver were solved by spatial filtering, and the waveguide loss was predicted to be roughly -0.4dB/μm for wavelengths between 1.4 and 1.6 μm. The silver slab was located on top of a silicon dioxide layer of 1.4 μm thickness, which was in turn supported by a silicon handle. 90% of its optical energy of the plasmon mode is contained in a region of about 1 square micron region at the edge of the silver slab. The entire geometry is clad in polymethylmethacrylate (PMMA), which is known to exhibit low optical losses in the near infrared regime [28]. The properties of silicon

waveguides formed by a .5 μm ridge waveguide with .12 μm thickness in such a system were also studied. Figure 4.1 shows simulation results for both modes. Both modes are primarily polarized with the E field parallel to the chip surface.

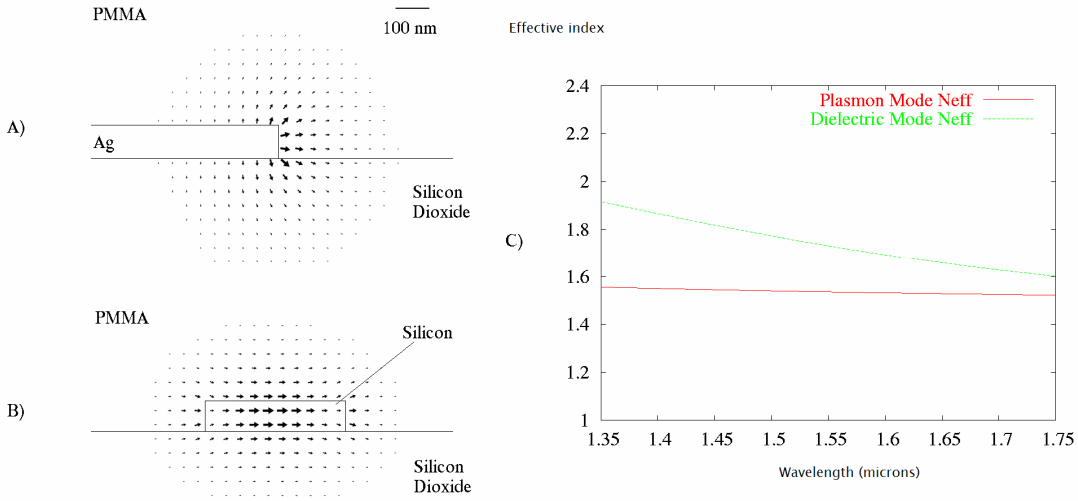

Figure 4.1. In A) and B) the E field vector components are rendered for the plasmon and silicon waveguides used in our study. C) shows the dispersion diagrams of both modes.

To construct optical circuits, SOI wafers were obtained with an approximately 120 nm thick top silicon layer and a 1.4 micron buried oxide layer. Dow Corning's HSQ resist [29] was spun onto the chip, baked at 170° C, and silicon waveguides were exposed at 100 kV in a commercial electron beam lithography system at 3500 μC/cm^2. After development, pattern transfer was performed using a chlorine ICP plasma [30]. For the metal layer, PMMA resist was again spun onto the surface of the chip, and 100 nm of silver was evaporated followed by a metal liftoff. Finally, a thick layer of PMMA was

spun onto the completed sample and baked – this layer served both as a water diffusion barrier in order to protect the silver from oxidizing and as a cladding layer for the waveguides.

Efficient coupling between plasmon and SOI waveguides was achieved by directional coupling. FDTD simulations predicted that a coupling length of 1.8 μm with a 150 nm separation between the plasmon and silicon waveguides resulted in broadband coupling efficiencies with a peak value of 2.4 dB at 1520 nm. In our simulations, it was found that the amount of light coupled between the silicon and metal waveguides oscillated as a function of the length over which they ran parallel to one another, which justifies our characterization of the coupling as directional in nature, as opposed to butt-coupling. Figure 4.2 shows the insertion loss as a function of wavelength, as well as a rendered image of the coupling simulation. Unfortunately, the coupling efficiency suffers greatly from small perturbations in the spacing between the silicon and plasmon waveguides, with FDTD predicted falloffs on the order of 3 dB for 50 nm of offset. The misaligned efficiencies are also plotted in Figure 4.2. Because of the high sensitivity to edge misalignment, our multi-layer fabrication had to be performed with a zebra mask by using repeated devices with intentional misalignments of ±50 nm in both Cartesian axes.

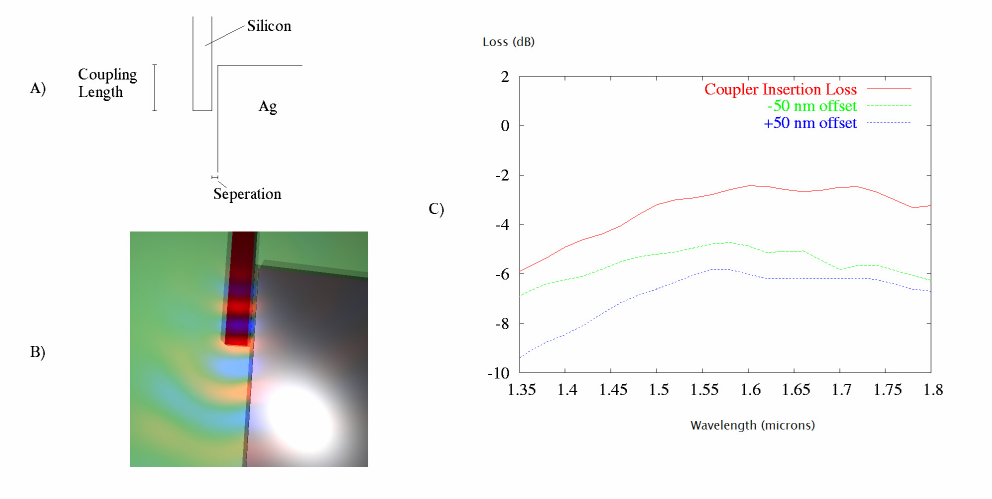

Figuer 4.2. A) shows a diagram of the layout of the dielectric plasmon coupling device. A rendering of a simulation is shown in B), while C) shows the simulated insertion loss for the coupling device in dB vs wavelength in μm. Also shown are the insertion losses when the coupling device separation is increased or decreased by 50 nm, as might happen due to misalignment in fabrication.

It is worth noting that the peak electric field for the plasmon waveguides is approximately $3x10^6$ V/m for 1 milliwatt of optical power. This is nearly identical to that seen in the Silicon ridge waveguide. Despite the somewhat concentrated nature of the mode at the edge of the metal layer, it is clear that there is not much field enhancement in this configuration, compared to other nanophotonic waveguides.

The waveguide loss of the plasmon waveguides is not good. It was found to be approximately 1.3 dB/um, by performing linear regressions on a series of waveguides of varying lengths. Clearly, any application involving these waveguides must involve relatively small regions of the waveguide. Moreover, the average insertion loss from the Silicon waveguide to the plasmon waveguide is not good; it was measured to be 3.4 dB.

4.3 Conclusions

It must be frankly stated that these results are of limited utility. It may be of interest to have demonstrated such guiding at all in a relatively unlikely choice of material for optical waveguides. However, the utility of plasmon waveguide based devices is not immediately obvious. With a waveguide loss of over 1 dB/um, only a device with sub micron functionality could really be viable. But it is not clear just what such functionality might be. One might consider functionalizing the metal, in order that a change in refractive index is brought on by exposure, for instance, to some kind of biological material. But such sensors typically operate with less than 1% shifts in the index of refraction. While it is possible to observe such a phase shift, it is probably far more convenient to build the sensor around a Silicon based waveguide, where a ring resonator can easily convert such a phase shift into a complete extinction of the optical signal.

One achievement that should be noted is that between the low loss directional coupler, and the efficient grating coupler, only about 10 dB of insertion loss exist on a fairly broadband coupling path (40 nm of bandwidth) from a standard telecom fiber to a nanoscale surface plasmon waveguide. It may be the case that there is an application for extremely small plasmon waveguides in the form of some sort of AFM imaging device, for instance. One might imagine a configuration similar to the one we have demonstrated here being involved in the process of coupling a large fiber mode down to a nanoscale AFM tip.

Chapter 5

Optical modulation with second order nonlinear polymers

5.1 State of the art in optical modulation

Broadly speaking, optical modulation can be described as the process by which a relatively low frequency signal, often in the regime of 1 MHz-100 GHz and carried on conventional circuitry, is transferred onto an optical signal at nearly 200 THz with amplitude modulation. But most modulators of commercial interest must function at least at or near 10 GHz. Only a few mechanisms operate quickly enough to reach the requisite speeds.

One mechanism commonly used in industry is that of nonlinear optical crystals that exhibit the Pockels effect, which refers to the change of refractive index in response to an externally induced field. Lithium Niobate exhibits such a nonlinearity, and is frequently used in commercial telecom modulators. [1] One drawback of such material systems, however, is that they are typically quite expensive to manufacture, requiring crystal growth.

Another approach is to use free-carrier modulation. This refers to the fact that a Silicon waveguide experiences a change in the index of refraction when a concentration of free carriers is introduced. This can then be used, in conjunction with a Mach-Zehnder

geometry, to accomplish modulation. This technique can achieve modulation speeds, even in Silicon, of up to 10 GHz [31].

A third type of modulator is based on the Pockels effect in nonlinear optical polymers. Perhaps the most important quality of nonlinear polymers is that they can be engineered and improved in ways that nonlinear optical crystals cannot. In fact, most nonlinear polymers typically have a larger nonlinear coefficient than comparable nonlinear optical crystals [36]. Also, nonlinear polymer can be easily integrated into a number of different optical systems, such as the Silicon waveguides described in this work. As a result, a great deal of flexibility is added to the engineering process. Also, as will be shown in the next chapter, exciting new applications are opened up with the use of this material in a nanoscale waveguide.

There have been a number of previous works demonstrating the use of second order nonlinear polymers to accomplish modulation. An excellent example is the work of Steier et al [32]; they were able to use low index contrast waveguides to form ring resonators, which were composed largely of second order nonlinear polymer material.

It is important to note that one of the most important figures of merit for a modulation scheme is how much shift in index of refraction is induced by a given voltage. If this number is exceedingly low, then several methods must be used to increase the performance. One possibility is to increase the input voltage. The first option leads to an increase in expense of the final device, and is not practical past 100 V for most applications in the RF regime, which is of course where the response of most materials is weakest. The second option is to increase effective device path length, in order to allow a longer period of interaction between the light and the index-shifted material. This too has

several drawbacks; ultimate device expense is increased due to the larger space required. Also, the design may be more difficult, as when the dimensions of the modulation region approach those of the RF wavelength involved, phase matching conditions must be met.

One of the problems with Steier's work, and indeed with most conventional modulation schemes, is that there is not an obvious path for increasing the response of the material to externally induced voltages, beyond simply obtaining material with a more pronounced nonlinearity. This is because typically the electrodes must be optically isolated from the waveguide region, and as the waveguide mode is quite large, this requires them to be separated by as much as 10 um, in the case of Steier's work. Similar limitations are found with lithium niobate based modulation systems [1].

One of the primary focuses of our work has been to attempt to overcome this limitation. The actual modulation achievable per unit voltage is proportional to the electric field experienced by the modulation region; so, if the electrodes are drawn closer together, in order to increase the amount of field experienced for a given amount of voltage, it is clear that this parameter can be improved. With the geometry that we will introduce, a path to achieving this will become apparent, and with the aid of this method, we will in fact show that nonlinear polymer based modulators with better performance can be obtained compared to Steier's results.

5.2 Silicon slot waveguides

It is clear that in the region of the waveguide, only a single voltage will be supported for a normal Silicon slot waveguide, such as was described in previous chapters. There is only a single conductive mass, and even if a voltage can somehow be induced via

external coupling, as described by the segmented waveguide, no field will be induced. This problem can be solved by establishing a waveguide geometry that has multiple, isolated electrical regions. An excellent example of one such structure, and one that we used in our experiments, is the Silicon slot waveguide. Figure 5.1 shows a cross section of the waveguide, as well as the modal profile and dispersion plot. For all of the experiments we performed, the two arms were 300 nm in size, while the center gap was 100 nm.

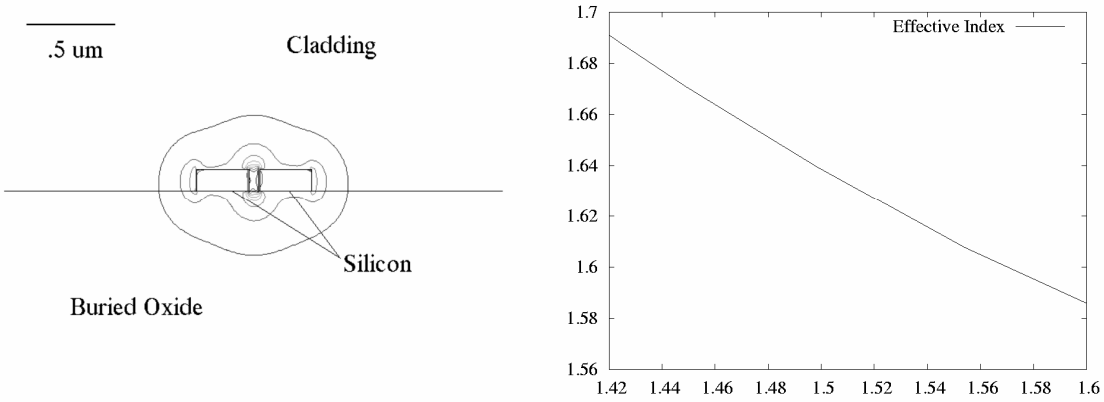

Figure 5.1: Slot waveguide mode profile, and effective index vs. free space wavelength in microns. The mode profile consists of |E| contours, plotted in increments of 10% of the max field value. The E field is oriented primarily parallel to the wafer surface.

This structure was first proposed by Lipson et al. [34] as a means to enhance the field intensity. It was argued that the abrupt shift from ε=11.56 in Silicon to ε=1 of air would produce a large electric field, at least in the horizontally polarized case (as we study here), because of the divergence-free nature of εE. However, such divergences can be found in ridge waveguides, and it in fact is the case that the peak E field for 1

milliwatt of power is still about $3x10^6$ V/m in this geometry. Moreover, there are several disadvantages to this geometry; we have found that fabrication is much more difficult, and the optical mode is apparently far more sensitive to surface roughness with this geometry [35].

In fact, the waveguide losses that are associated with this structure are not as low as that which can be obtained in ridge waveguides, though the fabrication and testing procedure is naturally nearly identical. Losses were at best -10 dB/um, compared to the previously quoted result of -7 dB/um for the ridge waveguides.

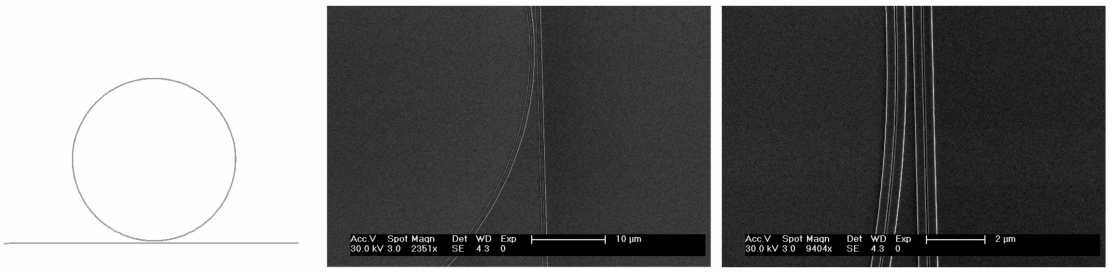

Figure 5.2: Device layout of ring resonator for waveguide loss characterization of split ring waveguide, and scanning electron micrographs of the slot waveguide oval and input waveguide. The entire oval is shown in the middle frame, while a detailed image of the coupling region is shown in the right frame.

It is worth noting that coupling into these slot waveguides is not straightforward. One cannot simply butt-couple them to a ridge waveguide as is possible with the segmented waveguides. Nor does directional coupling work; the differences in refractive index and modal distribution mean that very little of the radiation would be properly coupled. Instead, an adiabatic splitting is required. The actual coupling mechanism that

was used is shown in Figure 5.3. One may note that there is a region of periodically interrupted waveguide at the end of the splitting; this is there in order to preserve electrical isolation between the two halves of the slot waveguide.

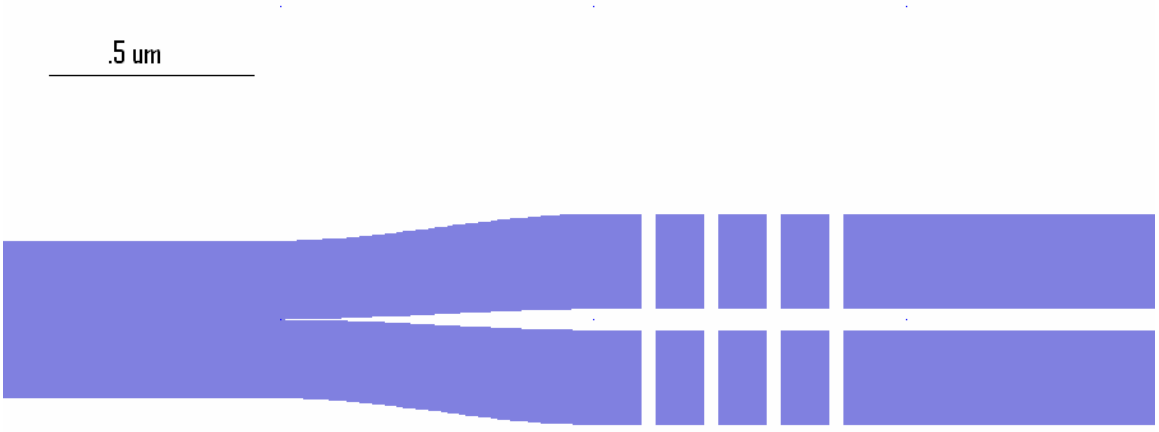

Figure 5.3: Device layout of the ridge-to-slot waveguide coupling device. A dark region indicates a region that is not to be etched in the Silicon, while the light regions indicate regions that are to be etched.

With the proper choice of both periodicity of the “Bloch isolation” region, and the proper adiabatic transition from ridge to slot, there is nearly no loss from this coupling region; measurements indicate the insertion loss is less than .5 dB. It is important to note, however, that all of these measurements were done with claddings having n of 1.5-1.7. Using an n of 1 causes these designs to stop working.

Before commenting on the nonlinear material itself, and the devices that made use of this material, it is useful to comment on the electric fields that could be produced with this device. Imagine that the left side of the waveguide was held at 0 V, while the right

side at 1 V; an electric field of 10 megavolts/m would exist across the gap. By contrast, if the electrodes were separated by 10 um, as might be typical in other modulation configurations, only .1 megavolts/m would be experienced. Of course, a significant amount of the optical power exists in the middle section of this waveguide. Moreover, the cladding material can deposit itself in the gap. All of these factors combine to make this waveguide demonstrate a significant amount of index shift in the cladding when exposed to a bias voltage.

Mention should be made here concerning the conductivity of the silicon. The silicon layer was doped to approximately 10^{19} phosphorous atoms/cm^3, yielding resistivities after dopant activation of ~0.025 ohm-cm.

5.3 Dendrimer-based nonlinear material

I would be remiss in not mentioning briefly the particular nature of the nonlinear polymer used. It was fabricated with the following technique, by collaborators at the University of Washington. [36, 37]. One of the challenges of using the nonlinear polymer was the need to spin the polymer on in a clean environment. This was done using a conventional photoresist spinner at the University of Washington. While a few experiments had the polymer applied to the chip at Caltech, the results obtained from this were never as good.

The process of poling the polymer should also be mentioned. Once the polymer had been spun on, it was still in an anisotropic state with a lack of second order nonlinear moment. To establish a preferred orientation, the polymer was heated and poled with a high voltage field by biasing the modulator. For further information on this process, refer to [38].

5.4 Ring resonator-based modulators

Once slot waveguides could be successfully built in Silicon-On-Insulator, and the nonlinear polymer spun on, several options were available in the choice of designs that would demonstrate modulation. The most obvious choice, a Mach-Zehnder interferometer, offered the usual advantages; it would be broadband, and in principle could be made long enough to demonstrate a nontrivial amount of modulation even in the face of monumentally bad performance. Also, the resulting device would be robust to shifts in temperature. However, there are substantial drawbacks to such a configuration. In the first place, because of the limited conductivity of the Silicon, there would be a substantial resistance experienced in current propagating for multiple centimeters down the waveguide. This, along with the capacitance of the Mach-Zehnder arm, would create difficulties driving an electrical signal through the arm at any kind of reasonable speed. A possible solution is to have a metal be coupled to each side of the waveguide through a bloch waveguide segmentation, similar to what has been proposed previously. However, since there is already some excess loss from the slot nature of the waveguide, further elaborations are likely to increase the loss to such a level that the Mach-Zehnder could not have reasonable overall insertion loss.

Another approach, and the one that was adopted here, was to use a series of ring devices to form the modulators. The basic approach is to arrange the layout so that a ring can be formed with a slot waveguide that has two distinct voltages, allowing the effective

index of the mode in the entire ring to be altered with an external bias. Figure 5.5 shows the layout, and an SEM image of the device.

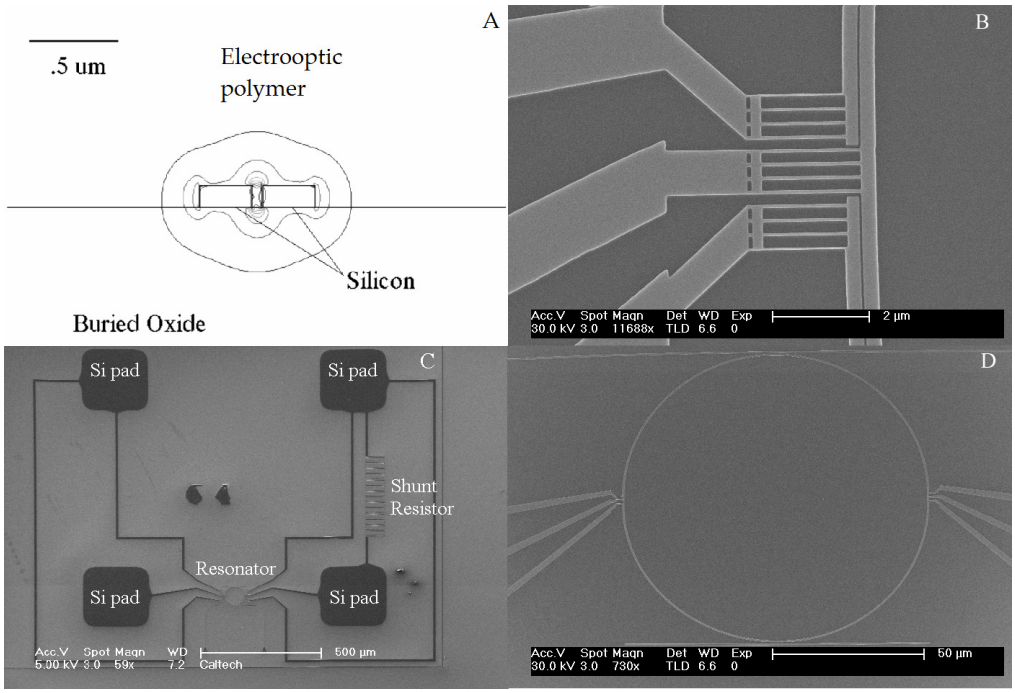

Figure 5.4: Panel A shows a cross section of the geometry with optical mode superimposed on a waveguide. Panel B shows a SEM image of the resonator electrical contacts. Panel C shows the logical layout of device, superimposed on a SEM image. Panel D is an image of the ring and the electrical contact structures.

As can be seen, a segmented waveguide region is utilized to enable direct electrical contact with the ring. The RC turn-on time for the entire ring device is estimated on the order of 100 MHz. This value could be greatly decreased by making the contacting arms shorter or thicker, or by doping the Silicon further. At DC, the Pockels effect was measured by applying varying voltages to the device and observing the device

transmission as a function of wavelength. For devices with working modulation, the resonance peaks were shifted, often to a noticeable degree. To counter the systemic drift due to temperature fluctuations, a series of random voltages were applied to a device under test and the wavelength responses noted. The intersection of a resonance peak and a certain extinction, chosen to be at least 10 dB above the noise floor, was followed across multiple scans. A 2-D linear regression was performed, resulting in two coefficients, one relating drift to time, and one relating drift to voltage.

At AC, a square wave input voltage was put across the device. The input wavelength was tuned until the output signal had the maximum extinction. It was determined what power levels were implied by the output voltage, and then the observed power levels were fit to a wavelength sweep of the resonance peak. This readily allowed the tuning range to be calculated. We successfully measured AC tuning up to the low MHz regime; the limitation at this speed was noise in our electrical driving signal path, not, as far as we can tell, any rolloff in the modulation process itself.

In Fig. 5.5, a result at approximately 6 MHz for the use of these structures as resonantly enhanced electrooptic modulators is shown. These experiments clearly demonstrate that low-voltage electrooptic tuning and modulation can be achieved in the same geometries as have been described for photodetection. It should be emphasized that these devices are not optimized as modulators. By increasing the Q of the resonators to exceed 20,000, which we have already shown, it will be possible to achieve much larger extinction values per applied voltage.

By utilizing new dendrimer-based electrooptic materials [36], we have achieved .042±.008 nm/V, or 5.2±1 GHz/V for these rings. This implies an r_{33} of 79±15 pm/V.

This result is substantially better than those obtained (0.8 GHz/ V) [32] for rings of 750 micron radius, which was the best tuning figure published to date in late 2005. By contrast, our rings have radii of 40 microns.

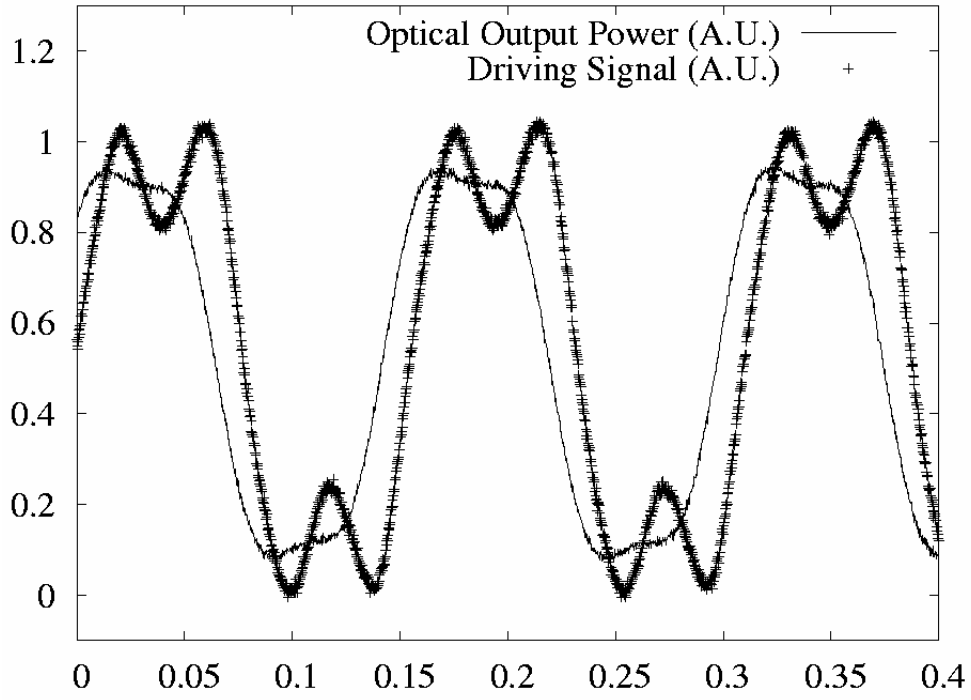

Fig. 5.5. Bit pattern generated by Pockels Effect modulation of a ring resonator at approximately 6 MHz. Peak to valley extinction was approximately 13 dB. The vertical axis represents input voltage and output power, both in arbitrary units. Horizontal axis is time in microseconds. Voltage swing on the input signal is 20 volts.

To summarize, based solely on a consideration of the modulation obtainable for a given voltage, there are clear advantages to be had in working with nonlinear polymers. It is also worth noting that the nonlinear polymers are increasing in strength compared to materials such as lithium niobate; the polymers studied in these experiments, for instance,

have an effective second order nonlinear moment, 110 pm/V, that is nearly double that of lithium niobate at 50 pm/V. Finally, it is worth noting that there is no intrinsic speed limitation with nonlinear poly based modulators. That is, as long as an RF (or higher) electric field can be supplied, the polymer will respond with modulation. This is in stark contrast to the free-carrier based modulator; for this type of device, carrier mobility and lifetimes become important, and typically limit performance to 40 GHz or less.

Chapter 6

Optical detection with second order nonlinear optical polymers

6.1 Theoretical background and motivation

Though the polymer was described as nonlinear in the last chapter, there was little involved with the modulation process that was, strictly speaking, an optical nonlinearity. As far as the optical signal itself was concerned, a ponderously slow electric field, changing at nearly one billionth of the optical frequency, simply altered the bulk properties of a material that then had a slightly higher refractive index. Aside from this "slow" DC or RF field, there is not a single nonlinear thing in the system. And, for some forms of modulation, such as free carrier or thermal modulation, that is in fact the end of the story, the only type of effect that can occur.

However, the nonlinear polymers that we have studied are truly optically nonlinear. They consist of an anisotropic material that responds to the optical signal as

$$D = \varepsilon_0(\varepsilon\ E + \chi^{\ 2} EE\ )$$

At large optical fields, the non-Pockels terms involved in the governing nonlinear equation cannot be neglected. For coherent input power, at a given location in the waveguide, the optical field is

$$E_{optical}(t) = A\cos(wt + \theta)$$

The term

$$E_{optical}{}^2 = \frac{A^2}{2}\cos(2(wt+\theta)) + \frac{A^2}{2}$$

will therefore contain not only frequency doubled components, but also a DC component. This phenomenon is known as optical rectification [40]. Because we have positioned electrodes (the two sides of the slot waveguide) at precisely the bounds of the induced field, the effect of optical rectification takes a small slice of the optical power and converts it into a virtual voltage source between the two arms. This in turn induces a current that we can measure and is linearly proportional to the input power $E_{optical}{}^2$.

Now let us consider the solution to Maxwell's equation in more detail. Our system can be approximated for this discussion as having two dimensions, with both the optical and DC electric field in the x direction and propagation in the z direction, for instance. Let us imagine that the χ^2 is nonzero and small for a tiny region from 0 to w in the x dimension. χ^2 is sufficiently small that the electric field due to the optical mode is still uniform. Let us imagine the system has no charge anywhere. The optical electric field can be written as $E = Ae^{ikz-iwt} + c.c.$ where c.c. indicates a complex conjugate. Let us further assume that the rectified DC field is of real amplitude C and uniformly directed in the x dimension on (0, w), and 0 elsewhere.

Other than the divergence condition, Maxwell's equations are still satisfied by this system. But at the edge of an interface on the interior, the DC frequency component of D_x, the displacement electric field, is discontinuous. At x=0, we have

$$D_x{}^- = 0$$

$$D_x^+ = \varepsilon_0(\varepsilon_r C + \chi^2 C^2 + 2\chi^2 \mid A \mid^2)$$

We neglect χ^2 C^2 because we expect the amplitude of the rectified field to be far smaller than that of the optical field. Clearly, the boundary condition of zero divergence can only be satisfied if Dx+ is 0. Then,

$$C = -\frac{2\chi^2}{\varepsilon_r} \mid A \mid^2$$

So we see that the direction of the rectified field is reversed compared to the direction of χ^2 . Note that there is no particular direction associated with the optical field as it is continually oscillating. As we have seen, this rectified DC field would then, if acting as a virtual voltage source, create an effective positive terminal on the positive polling terminal.

6.2 Ring resonator-based detector

The aforementioned ring resonators also serve, without any change, as detectors. Testing was performed with single-mode polarization maintaining input and output fibers, grating coupled to slotted waveguides with an insertion loss of approximately 8 dB. Optical signal was provided from an Agilent 81680a tunable laser and in some cases an erbium-doped fiber amplifier from Keopsys Corporation. A continuous optical signal inserted into a poled polymer ring results in a measurable current established between the two pads, which are electrically connected through a pico-ammeter. In the most sensitive device, a DC current of ~1.3 nA was observed, indicating an electrical output power of ~10^{-9} of the optical input power ($5\text{x}10^{-12}$ W of output for approximately .5 mW coupled

into the chip). Control devices, in which PMMA or unpoled EO material was substituted, show no photocurrent.

The fact that there is no external bias applied to this system or indeed any energy source, other than the optical signal, demonstrates conclusively that power is being converted from the optical signal. To establish that the conversion mechanism is actually optical rectification, we performed a number of additional experiments. First, we applied a steady bias on the chip for several minutes, as shown in Table 1A, and observed a substantial change in the photoresponse of the device. This change depends on the polarity of the bias voltage, consistent with the expected influence of repoling of the device in place at room temperature. Specifically, if the external bias was applied opposing the original poling direction, conversion efficiency generally decreased, while an external bias in the direction of the original poling field increased conversion efficiency.

Part A:

Action	New Steady State Current (6 dBm input)
Initial State	-5.7 pA
+10 V for 2 minutes	0 pA
-10 V for 2 minutes	-7.1 pA
+10 V for 2 minutes	-4.4 pA
+10 V for 4 minutes	-6.1 pA
+10 V for 4 minutes	-4.5 pA
-10 V for 2 minutes	-14.8 pA

Part B:

Device	Action	Current Polarity of Optical Rectification
1	Positive poling	Positive
1	Thermal cycling to	Rapid

	poling temperature with no voltage	fluctuation, did not settle
1	Negative poling	Negative
2	Negative poling	Negative
2	Thermal cycling to Poling temperature with no voltage	None observable
2	Positive poling	Negative
3	Negative poling	Negative
4	Positive poling	Positive
5	Negative poling	Negative

Table 6.1: Part A shows the dependence of the steady state observed current after room temperature biasing with various voltage polarities for one devices. The device was originally polled with a -12 V bias, though at 110 C. With one exception, applying a voltage in the direction of the original polling voltage enhances current conversion efficiencies, while applying a voltage against the direction of the polling voltage reduces the current conversion efficiencies. It should be noted that the power coupled on-chip in these experiments was less than 1 mW due to coupler loss. Part B shows the behavior of several different devices immediately after thermal polling or cycling without voltage. Measurements were taken sequentially from top to bottom for a given device. The only anomaly is the third measurement on device 2; this was after significant testing, and the current observed was substantially less than was observed in previous tests on the same device. We suspect that the polymer was degraded by repeated testing in this case.

To further understand the photoconversion mechanism, five EO detection devices were poled with both positive and negative polarities, thus reversing the direction of the relative χ^2 tensors. For these materials, the direction χ^2 is known to align with the polling E field direction [32], and we have verified this through Pockels' effect measurements.

In all but one case, we observe that the polarity of the generated potential is the same as that used in poling, and the +V terminal during poling acts as the -V terminal in spontaneous current generation, as shown in Table 1B. Furthermore, the polarity of the current is consistent with a virtual voltage source induced through optical rectification. It should be noted that these devices decay significantly over the course of testing, and that in one case the polarity of the output current was even observed to spontaneously switch after extensive testing. However, their initial behavior after polling seems largely correlated to the χ^2 direction.

A number of experiments were performed to produce negative results, and to exclude the possibility of a mistaken measurement of photocurrent. The power input to the chip was turned on and off by simply moving the fiber array away from the chip mechanically, without changing the circuit electrically, and the expected change in the electrical output signal of our detector was observed. A chip was coated in polymethylmethacrylate and tested, resulting in no observed photocurrents. Also, we tested some of the devices shown in Table 1 before any polling had been performed; no current was observed.

To establish a quantitative relationship between the laser power in the EO material and the photocurrent, we used a lock-in amplifier, and achieved a noise floor of about 0.2 pA. This resulted in a reasonable dynamic range for the 10-200 pA photocurrent readings. Figure 6.1(A) and 6.1(B) show optical transmission curves for typical devices. Figure 6.1(C) shows several traces of output current versus input laser power, and a fairly linear relationship is observed. The relationship $I = cP$, where I is the output current, P is the input laser power, and c is a proportionality constant ranging from

88 +/- 10 pA/mW at a 1 kHz lock-in measurement and when the wavelength is on resonance, changing to a lower value of 58+/-8 pA/mW off resonance for our best device. It is important to note that current was easily observed with only a pico-ammeter, or by simply connecting an oscilloscope to the output terminal and observing the voltage deflection.

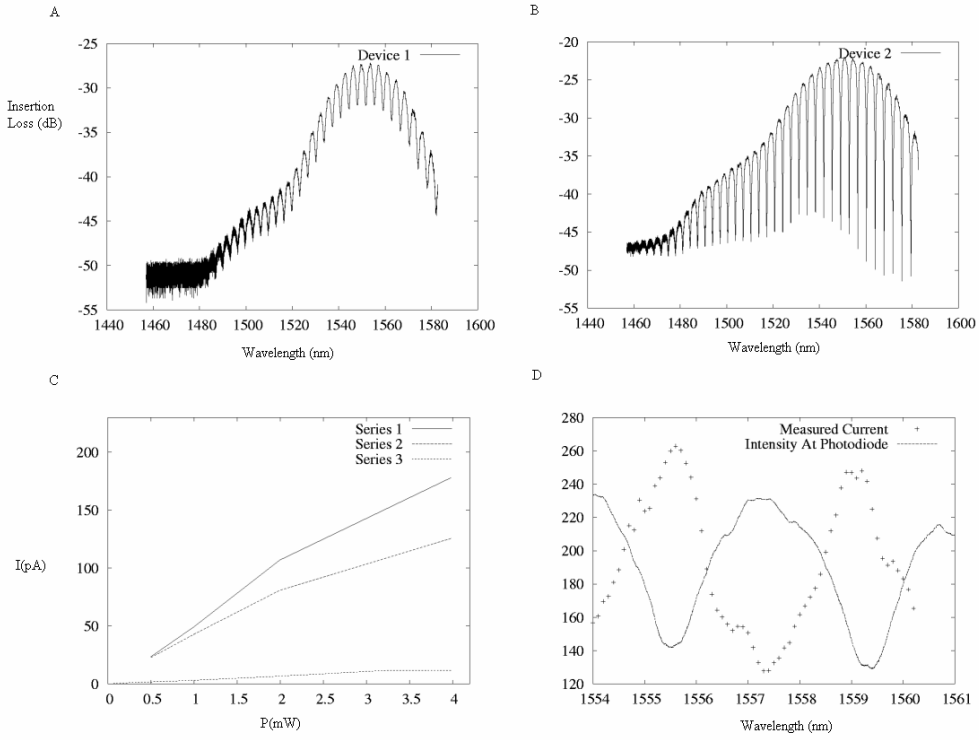

Figure 6.1: Panel A shows the transmission spectrum of detector device 1, whereas B shows detector device 2. Panel C shows several curves of current vs. power for three measurement series. Series 1 is of the first device with the wavelength at 1549.26 nm, on a resonance peak. Series 2 is the first device with the wavelength at 1550.5 nm off resonance. Series 3 is for device 2, with the wavelength at 1551.3, on resonance. Finally, panel D shows the output current as a function of wavelength, overlaid with the

transmission spectrum. The transmission spectrum has been arbitrarily rescaled to show the contrast.

As another demonstration of the dependence of the output current on the amount of light coupled into the resonator, we also tuned the laser frequency and measured the output current. As can be seen in Fig. 1(D), the amount of output current increases as the laser is tuned onto a resonance peak. This again indicates that the overlap between the EO polymer in the resonator and the optical mode is responsible for the photocurrent. We have overlaid a photocurrent vs. wavelength response scan to show the resonance peaks for comparison. It should not be surprising that a small photocurrent is still measured when the laser is off resonance, since the amount of radiation in a low-Q ring resonator is non-negligible even off resonance. It is also worth noting that we have successfully observed this detector function at speeds up to 1 MHz, without significant observable rolloff. This is again consistent with optical rectification. Unfortunately, our devices could not be measured at higher speeds, due to substantial output impedance.

The conversion efficiency from our first experiments is certainly several orders of magnitude below the ultimate limit, and can be explained by the high insertion losses in our system. 75% of the input power in the fiber is not coupled onto the chip and our low-Q resonators only provide a limited path length within which light can interact with the electrooptic material. Furthermore, by design a great deal of the light in the resonator will be dumped to an output port, and not absorbed. It is expected that with further design and higher-Q resonators, the efficiency of these devices can be greatly increased. It is, however, important to note that nothing about this effect depends on the presence of rings. The rings provide a convenient and compact device for observing these effects, but

one could just as easily observe optical rectification by using a long, polymer coated, split waveguide, with each side connected to an electrical pad.

6.3 Future work and scaling observations

There are several features of this detector that make it very interesting. First, there is the fact that there is no intrinsic speed limit. After all, the nonlinear polarization of the material is oscillating at the optical frequency! So, as soon as there is an intensity change in the optical signal, it can be "detected" in the form of a (relative) low frequency electric field that is induced. Of course, for extremely high frequencies, capturing this signal is no mean feat, and substantial electrical engineering would need to be done for this to function at, say, 10 GHz. But the exciting fact is that this detector may provide a cheap solution to the problem of detecting intensity modulated optical signals at extremely high speeds.

Secondly, there is no external power source that is required to make the detector work. First, this raises the possibility that the detector could actually act as some sort of power converter. Though the efficiencies that would exist currently render it uninteresting, improvements in the conversion process might make this possible. But more significantly, this may mean that for low noise measurements, this detector is superior to, for example, a reverse biased photodiode. After all, one of the main noise factors for many detectors, the dark current, is nonexistent for this detection method.

To consider how the detector can be improved, it is useful to analyze the amount of power that can be captured from the optical field in the presence of any enhancement in the electric field. Such enhancement might be achieved by a resonance process. The

ultimate power is proportional to RV^2, where R is the resistance across the optical gap. However, the voltage is proportional, as was shown above, to the square of the E field. So, we reach the surprising fact that the power that can be harvested from the detector goes as E^4! This means that even a relatively small resonant enhancement means that the detector may be able to function at much higher efficiency.

Chapter 7

Ultrafast modulators in silicon

7.1 Overview of relevant nonlinear optics

Nonlinear optics has been a field of great interest for over 20 years. There is a very wide variety of nonlinear optical devices that have now become critical tools in nearly all fields of applied science.

Because most nonlinear optical devices rely on relatively long path lengths or resonant field enhancement, it has proven quite difficult to create massively integrated nonlinear optics in the same way that transistors have allowed the integration of massively integrated nonlinear electronic devices. A critical step toward the construction of such integrated nonlinear optical systems is to demonstrate the ability to do ultrafast nonlinear optics with devices that can be constructed within the constraints of a planar, compact chip. There has been substantial work on attempting to integrate nonlinear optical devices in III/V semiconductor chips, but relatively little work on doing the same types of devices within a silicon-electronics compatible materials system.

The last several years have had an explosion of interest in integrated optical devices in silicon. Various groups have demonstrated lasers, muxes, electro-optic modulators, detectors, high-Q ring resonators, and a wide variety of other linear optical components. However, there has been very limited work done to date on designing and demonstrating integrated nonlinear devices. Because of the great benefits in terms of

cost and robustness of lithographically defined chip-scale technologies, and the remarkably advanced manufacturing technologies available in silicon, it would be extremely desirable to be able to construct ultrafast nonlinear optical devices within a silicon-compatible system.

The great problem with nonlinear optical effects is that they are quite small. In this work, we take advantage of the third-order nonlinear coefficient, which produces effects like cross-phase modulation and four-wave mixing. The strength of the third order nonlinearity in a given material is labeled as χ_3, which represents the coefficient on the third term in the Taylor expansion for the **D** field [41]:

$$D = \varepsilon_0(\varepsilon_r E + \chi_2 E^2 + \chi_3 E^3)$$

In fibers, nonlinear optical devices are often comprised of spools of fiber several kilometers long, because the optical loss is characterized in dB/km. In silicon integrated optics, we are not quite so lucky; losses are typically between 1 and 5 dB/cm [1]. Because the performance of a third order nonlinear device depends on the cube of the E field, this means that increasing device length beyond a few millimeters is of little value. So the critical question is whether it is possible to somehow enhance the strength of these nonlinearities without increasing the length of the devices.

Broadly speaking, there are three approaches to enhancing such nonlinearities. First, one can construct a resonant device, where energy has to pass many times through the system. Although this will in fact enhance the fields, it has the severe disadvantage of greatly reducing the bandwidth of the system. A typical high-Q resonator, which we can

build with a Q of 100,000 will give an 8x factor in terms of field enhancement. But the bandwidth of such a device is only about 2 GHz – definitely not something that can take advantage of ultrafast optical effects, which operate with femtosecond response times. Another significant disadvantage to such an approach is that the device will only work at discrete wavelengths, and be very sensitive to the temperature of the device. This is a particular problem, as high powers in a small area may well heat a device!

7.2 Silicon waveguides with nonlinear polymer claddding

As mentioned before, our waveguides have the property of enhancing the electric field of the optical mode, at least when compared to that which might be found in a fiber mode. By cladding our standard ridge waveguide with a nonlinear optical polymer, we can enhance the effective nonlinearity of the waveguide.

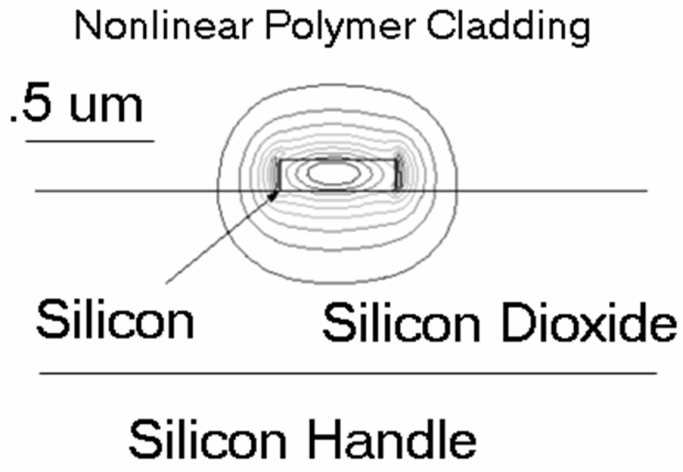

Figure 7.1: Diagram of waveguide layout and location of nonlinear polymer cladding.

By utilizing these advantages, we demonstrate here that it is possible to design and construct ultrafast nonlinear optical devices in silicon. Because these devices are non-resonant, they provide extremely high bandwidth. And since they take advantage of advanced nonlinear polymers spin-coated on top of the silicon waveguides, they benefit from the rapid progress being made in these new engineered optical materials.

Earlier in this thesis, optical rectification based detectors were shown – these rely on ultrafast nonlinear effects, but are not in and of themselves devices with ultrafast response times. Another class of devices, an all-optical modulator with response speeds of over 2 Terahertz, has been demonstrated. Being the first device of its class, it provides a proof that integrated nonlinear optics in silicon are a practical reality. We can expect similar devices to provide a wide variety of new functionality over the next several years, including integrated pulse reshaping and wavelength conversion functions. With more advanced designs, it may in fact prove possible to produce devices that exhibit signal gain, allowing for the construction of optical ”op-amps” and optical transistors – devices that allow a low-power beam of light to control a higher power one.

A word should be said concerning the nonlinear polymers used here. It was obtained from the Dalton group at the University of Washington, and is described further in [42]. In practice, it was simply spun on in a manner similar to photoresist, atop already fabricated Silicon devices.

7.3 Design of the amplitude modulator

Using just a single waveguide, and an optical spectrum analyzer (OSA) it was possible to characterize the approximate strength in the nonlinear optical materials by observing the behavior of four-wave mixing. Once we had characterized the properties of the materials available to us, the next step was to build an integrated amplitude modulator. The basic approach taken was to use a length of waveguide as an optically controlled phase modulator, and to have this length of waveguide comprise half of a Mach-Zehnder interferometer for the signal to be modulated (the source). The optical control signal (the gate) is combined onto one arm of an unbalanced MZI, causing a phase delay in that arm when the gate signal is on, since the total optical path length is slightly increased by the action of the third order nonlinearity. When the two halves of the source signal are recombined at the end of the MZI, they are slightly dephased by the action of the nonlinearity in one arm, thus causing a decrease in the output power of the MZI at the source wavelength [3].

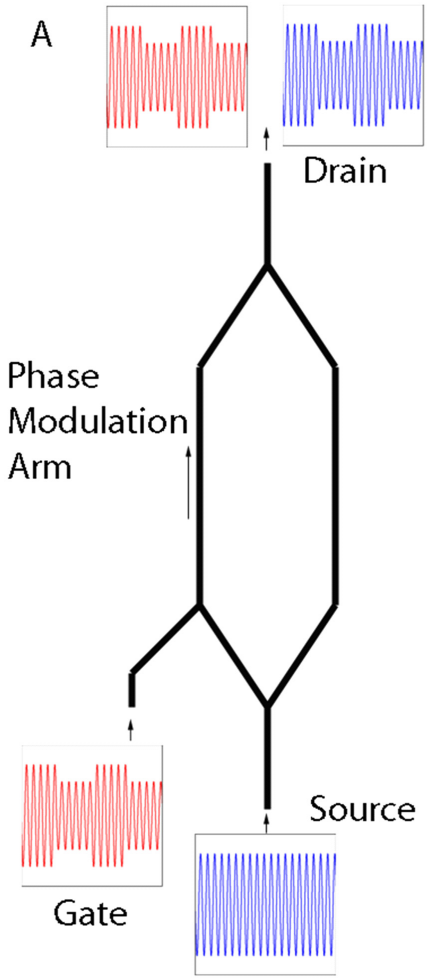

Figure 7.2: Logical device layout, as well as the actual layout of the device as designed.

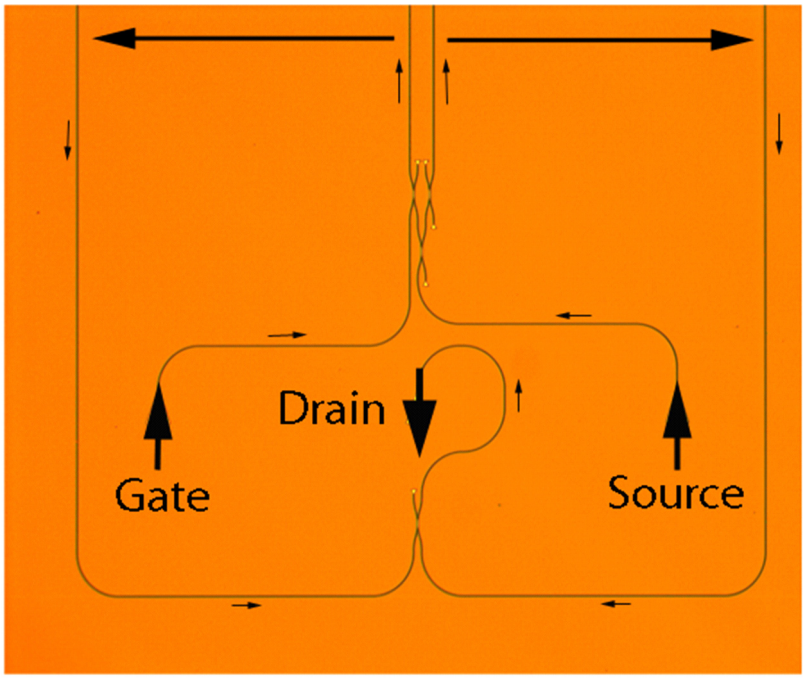

Figure 7.3: Optical image of fabricated device with light flow drawn in.

There were several key challenges in designing this device. First of all, it was necessary to design an extremely reliable, repeatable optical splitter and mux. Two splitters are needed – one to split the source wavelength, and another to recombine it at the end of the MZI. Only one mux is required, on the modulation arm – but two are used, in order to balance out the optical losses within the MZI. Also, because it was desirable to be able to use multiple nonlinear optical materials, it was necessary that the approach be largely insensitive to the exact cladding index of refraction. In fact, it was found that the easiest and most reliable way to do both the wavelength combining and the splitting was to simply use a directional coupler designed for 50% splitting across a wide input spectrum.

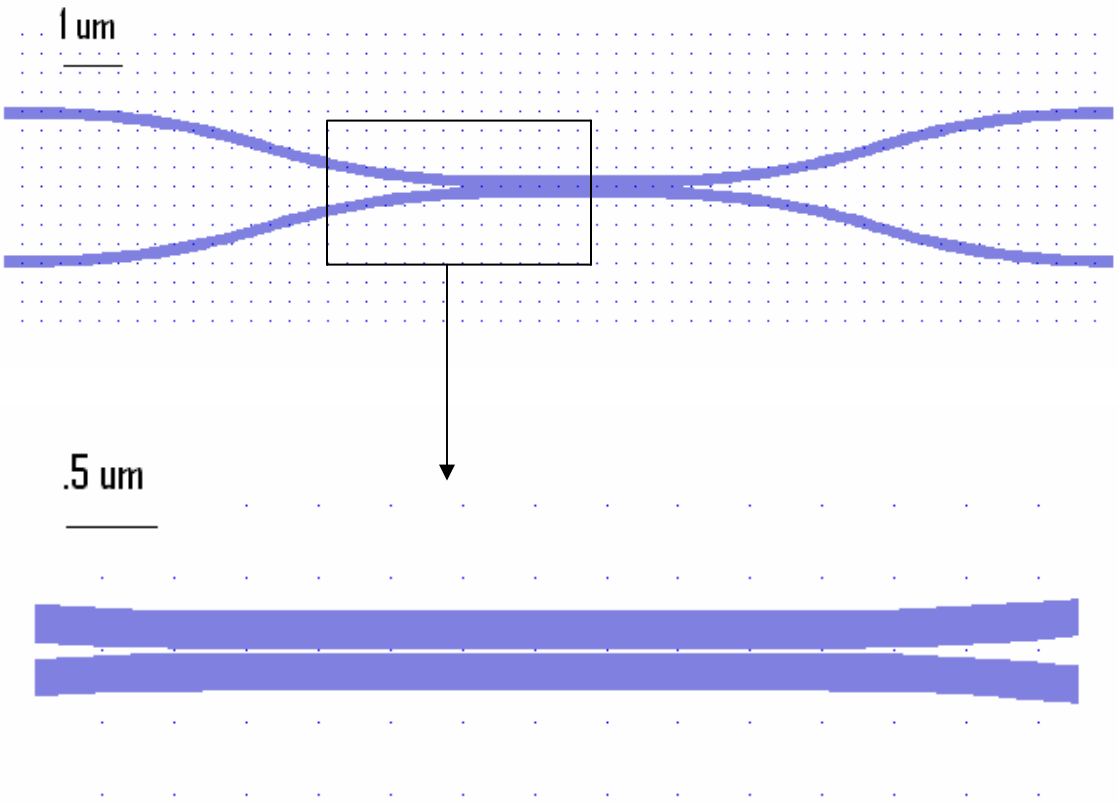

Figure 7.4: Layout of directional coupler designed to couple 50% of the optical mode from one waveguide to the next, near 1550 nm free space wavelength.

Also of note in the designs is the fact that the MZI used was deliberately unbalanced – one arm is 1.2 cm long, while the other is 1.24 cm. This allows us to change the bias point of the modulator and trade modulation depth against insertion loss. The passive spectrum of a typical device is shown.

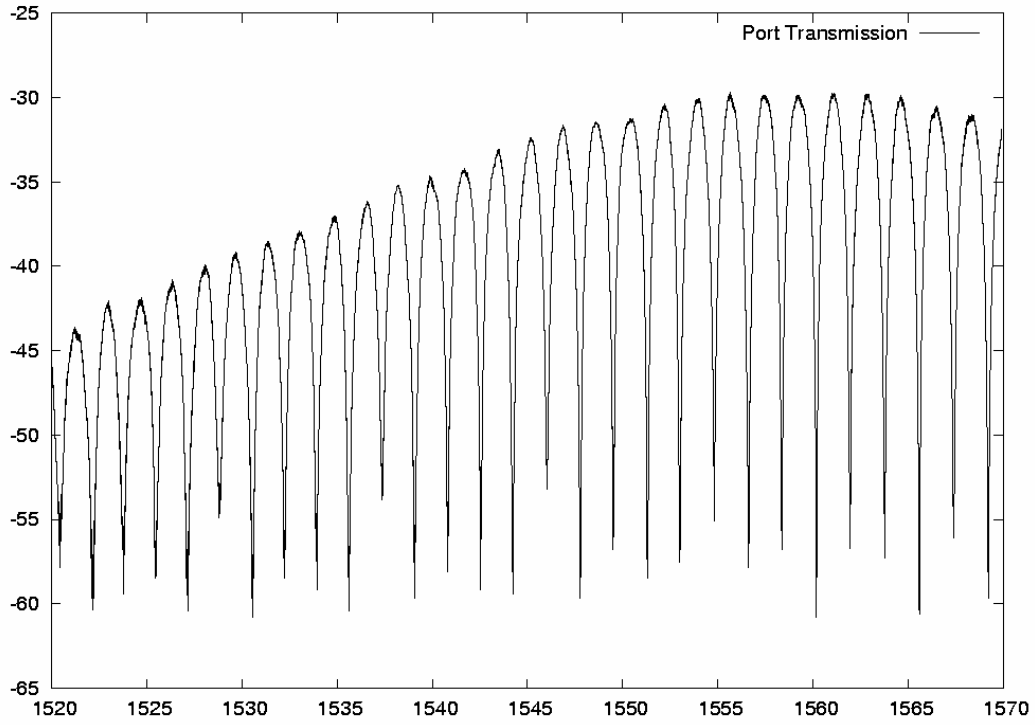

Figure 7.5: Transmission of source to drain on typical MZ device. Transmision is plotted in dB vs. laser wavelength in nm.

To best understand the limitations of the nonlinear phase modulation mechanism central to these devices, one must consider both the waveguide loss and dispersion of our waveguides. Together, these two parameters establish a limitation on the amount of phase shift that can be obtained, or the rate of change of the phase shift that can occur. Our waveguide loss has been extensively calibrated through other test structures, and is known to be -7 dB/cm. The effective index of these waveguides near 1550nm is well modelled by

$$n_{eff}(\lambda) = 1.91 - 1.09 * (\frac{\lambda(nm) - 1550}{1550})$$

One can refer to the dispersion plot given in chapter 3. The limitations on the nonlinear response can be best characterized by introducing the concept of effective length. The effective nonlinear length of a given waveguide is the equivalent length of a lossless, dispersion free waveguide. For a modulation frequency of ω_m, the effective length can be written as

$$Leff(\omega_m, \alpha, L) = \left| \frac{\exp(-2\alpha L)\exp(-2i\frac{L}{c}\frac{\partial n}{\partial \omega}\omega_m{}^2) - 1}{-2i\frac{1}{c}\frac{\partial n}{\partial \omega}\omega_m{}^2 - 2\alpha} \right|$$

It can be shown that for our waveguides, an asymptotic value for L_{eff} of 0.5 cm is approached for L > .7 cm. It turns out that ω_m must approach 10 THz before any significant change in effective length occurs. This indicates that our device has an operation speed that can exceed the measured 2.6 THz, and approach 10 THz, and that the current limitation on device performance is the waveguide loss.

A model for the performance of these devices was developed, starting with the same equations used above for four-wave mixing, but modified slightly for the dispersive nature of the waveguide [43]. Here $\chi 3$ is in $(m/V)^2$.

$$\left(\frac{\partial^2}{\partial z^2} - \frac{1}{(c/neff)^2}\frac{\partial}{\partial t^2}\right) Ex(z,t) = \frac{1}{c^2}\frac{\partial^2}{\partial t^2}(\chi^3 Ex^3)$$

Where Ex is the collection of all modes:

$$Ex = \sum a_i \exp(ik_i z - i\omega_i t) + a_i * \exp(-ik_i z + i\omega_i t)$$

Note that Ex is always real valued, as is required for use with the equations of nonlinear optics. Using the standard slowly varying amplitude approximation, all of the linear terms are assumed to vanish for propagating modes, except for

$$\sum 2ik_i \frac{\partial a_i}{\partial z} \exp(ik_i z - i\omega_i t) + c.c. = \frac{\chi^3}{c^2} \frac{\partial^2}{\partial t^2} Ex^3$$

Proceeding further depends on the particular nonlinear process under study. In the case of energy conversion by four-wave mixing, taking ω_2 as the generated frequency, and ω_1, ω_0 the pump beams, when ω_2=2ω_1-ω_0, we have

$$2ik_2 \frac{\partial a_2}{\partial z} \exp(ik_2 z) = \frac{\chi^3}{c^2} 3(-i\omega_2)^2 a_1{}^2 a*_0 \exp(2ik_1 z - ik_0 z)$$

$$a_2(L) = -\frac{i3\omega_2{}^2 \chi^3}{2c^2 k_2} a_1{}^2 a*_0 \int_0^L \exp(i(2k_1 - k_0 - k_2)z) dz$$

The final term, however, is simply a measure of the so-called momentum mismatch between the three waves. As we have shown elsewhere, for our waveguide at length scales around 1 cm, and for frequencies less than 10 THz, this mismatched value is not significant, and the integral is nearly equal to L.

Under this assumption ($|a_1|=|a_0|$), and under the condition that the two laser beams are nearly equal in power, the experimentally measured *f* fraction is then

$$f = \frac{|\, a_2(L)\,|^2}{|\, a_1\,|^2} = \left(\frac{3\omega_2{}^2\chi^3}{2c^2k_2}\right)^2 L^2\,|\, a_1\,|^4$$

In the case where one beam (ω_2) is intensity modulated by another beam (ω_1), the process can be written as

$$2ik_2\frac{\partial a_2}{\partial z}\exp(ik_2z) = \frac{\chi^3}{c^2}6(-i\omega_2)^2\,|\, a_1\,|^2\; a_2\exp(ik_2z)$$

$$a_2(L) = a_2\exp\left(\frac{-i6\omega_2{}^2\chi^3}{2c^2k_2}\right)L\,|\, a_1\,|^2)$$

It is seen that, as seen by beam 2, propagation amounts to multiplication by a complex value with modulus 1. The absolute value of the argument of this value is readily seen to be twice f. That is,

$$\Delta\phi = |\arg(\exp\left(\frac{-i6\omega_2{}^2\chi^3}{2c^2k_2}\right)L\,|\, a_1\,|^2))\,| = 2\left(\frac{-i3\omega_2{}^2\chi^3}{2c^2k_2}\right)L\,|\, a_1\,|^2 = 2\sqrt{f}$$

Finally it will be noted that the expression used in the paper was twice this: $4\sqrt{f}$. This is because the measured f is artificially suppressed by a factor of ¼ due to passing through the final 3dB coupler – the produced sideband is reduced 3 dB, while the signal laser, since we biased the Mach-Zehnder at max, is magnified by 3 dB.

7.4 Experimental overview

The devices were first tested optically in order to establish their passive performance, in the low-power regime. Refer to Figure 4 for a typical transmission plot. As with all of our optical results, there is both fine and broad structure. The broad structure is attributable to the out-of-plane couplers, which allow the devices to be directly coupled to single mode optical fibers. The narrow structure on Figure 4 is the result of the Mach-Zehnder Interferometer being unbalanced. Using this unbalanced interferometer allows the performance of the device to be tuned by changing only the wavelength – by operating near the peaks, it's possible to optimize for high optical power throughput, but low modulation. By operating with the source wavelength at the high-derivative points, it is possible to have much higher modulation depth for a given change in the input gate power, but this engenders significant additional optical loss.

Two types of experiments were performed in order to characterize the performance of the terahertz modulators: First, a series of experiments was done in order to characterize the devices' performance at ultrafast speeds. These took advantage of an OSA as the detector, since no electrical test methodology provides Terahertz of detection bandwidth. Although the data collected in this experiment would have been sufficient to understand the behavior of the devices, the spectral locations of all of the generated peaks are identical to those generated by four-wave mixing. Only by observing changes in the magnitudes of the peaks (detailed below) could the performance of the devices be distinguished from a pure phase modulator, since an optical spectrum analyzer gives power measurements but not measurements of phase.

The second set of experiments was performed at Gigahertz speeds, and took advantage of the ability to directly measure both amplitude and phase of signals at these speeds. By using a vector network analyzer connected to both an optical modulator and a diode detector, it was possible to both excite and detect the behavior of the devices at Gigahertz speeds. Because the detectors used in this experiment are sensitive only to changes in optical power, this provided a key confirmation that we were in fact observing amplitude modulation. The agreement between the values for the magnitude of the modulation from the gigahertz to the terahertz also provides a powerful verification that the two experiments were correctly analyzed.

In all cases, negative case experiments were performed using PMMA cladding in lieu of the nonlinear chromophore cladding. These showed greatly reduced nonlinear effects, as expected.

7.5 Two-laser modulation experiment

The terahertz experiments, which show that these devices have measurable modulation response up to 2.5 terahertz, were performed using three lasers, each operating at a different wavelength. The first two, $\lambda 0$ and $\lambda 1$, are combined off-chip with a polarization maintaining 3 dB splitter and then amplified by an erbium-doped fiber amplifier (EDFA). These two lasers together are fed into the gate port on the device, and comprise the gate signal. Two lasers are necessary in order to obtain a modulation envelope at their difference frequency, through linear superposition of the two fast signals. This difference frequency is what is used as the test tone for these ultrafast experiments.

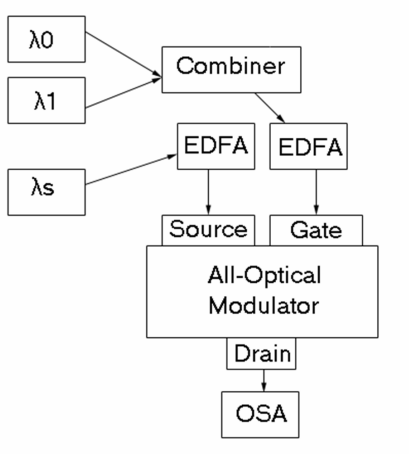

Figure 7.6: Logical layout of two-laser modulation experiment.

The third laser, λS, is also fed through a separate EDFA and subsequently into the source port on the modulator device. The EDFAs are required because the couplers fabricated on-chip are relatively inefficient, and lose several dB of optical power. The critical power levels for evaluating this work are the power levels at the inputs to the devices, since with better couplers it is these power levels that will dictate the practical applicability of devices like the ones presented herein. For these experiments, the power level at the beginning of the phase modulation arm (where the gate wavelength is combined) was 14 dBm in each of the gate wavelengths, and 10 dBm at the source wavelength. These power levels are well within the range where single-mode semiconductor lasers are commercially available today.

In these all-optical experiments, the output from the drain port is routed to the optical spectrum analyzer. By varying the spacing between the two gate lasers, it is possible to vary the modulation frequency. Shown in figure 7.7 are three different measurements with modulation at 2.5, .6, and .25 THz. 2.6 THz was the highest frequency of modulation that could be conveniently observed, because of limitations on

the bandwidth of the optical couplers. It is estimated that these devices in fact are capable of operation to speeds of approximately 10 THz, with the performance being ultimately limited by phase mismatch due to waveguide dispersion.

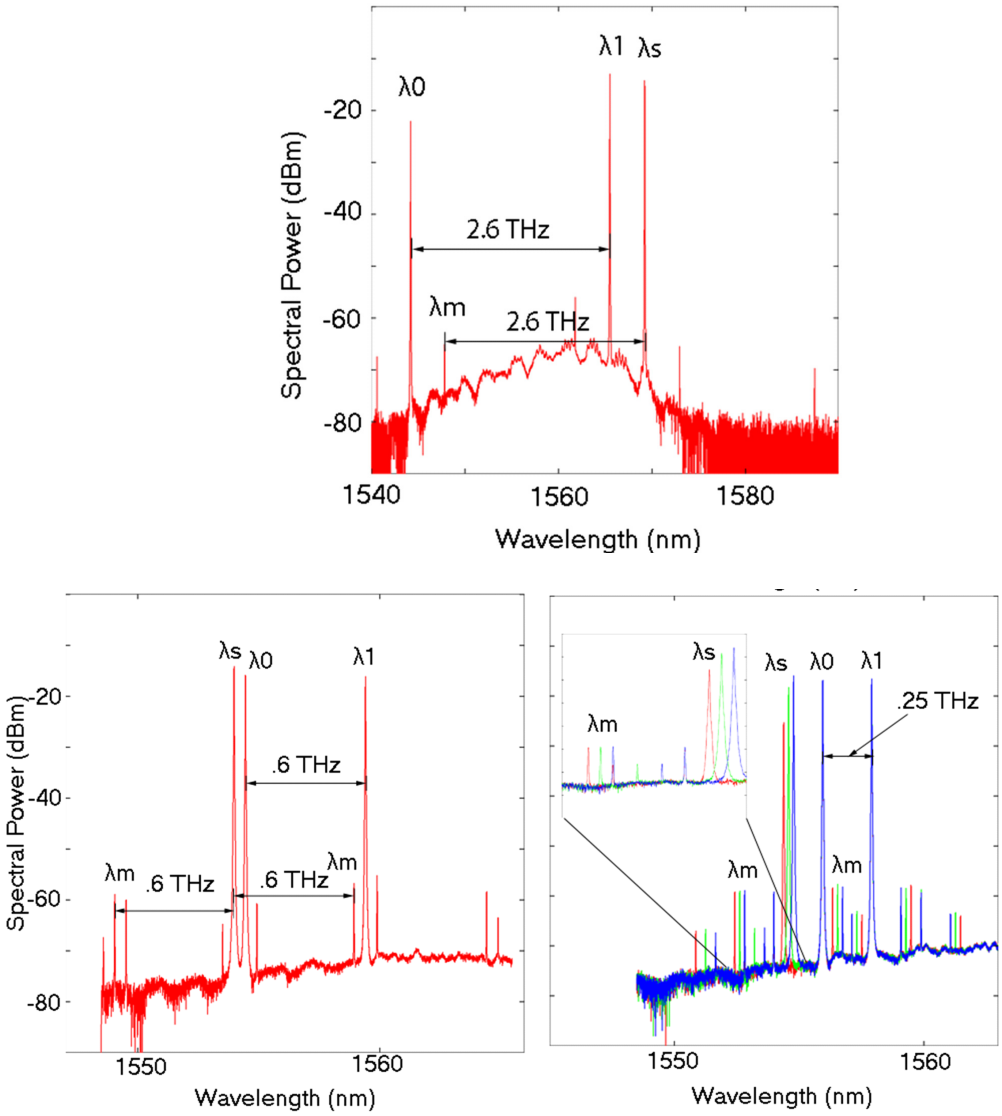

Figure 7.7: Results of two-laser modulation experiments, with varying separations between the two gate lasers.

Figure 7.7 Panel C shows a series of scans taken with the source wavelength being varied. It is critical to observe that while the throughput at the source wavelength changes as the wavelength is varied, the height of the sidebands does not change. This is a signature of amplitude modulation, and is a feature that distinguishes this result from the results of pure four-wave mixing. In an FWM experiment employing a single waveguide, the height of the modulation sidebands would decrease along with the source throughput. Because the device used here is an unbalanced MZI, the tuning of the source wavelength results in a change in the relative phase of the light being combined at the downstream end of the MZI, and thus in a change in the output power. The height of the sidebands does not change because varying the source wavelength does not change the amount of power in the modulation arm of the MZI. The amount of phase modulation of the source does not depend on the wavelength of the source, so the height of the modulation sidebands remains unchanged as the source wavelength is changed.

One may comment that the results of these experiments do not look much different from those due to simple four-wave mixing in a single waveguide. That is because, as far as the frequency content of the output radiation is concerned, there is nearly no difference between the two scenarios. This is a feature of all Mach-Zehnder modulators; the only part of the device that is actually nonlinear is the arms. The coupling regions simply combine optical signals in a linear fashion. But we do not think of a Mach-Zehnder as a phase modulator simply because it looks identical to one in the frequency domain, and so neither should this device not be considered a four-wave

mixing device. Of course, it is in the time domain that any amplitude modulation is truly observed, and we have devised an experiment to test just this.

7.6 Direct intensity detection measurements

Because the previously described all-optical measurements do not provide a way to directly measure the amplitude modulation of the output, a second set of experiments was performed. The goals were twofold: First, to confirm the results of the all-optical experiments with a completely different experimental setup. Second, to show unambiguously that what is being observed is amplitude modulation with a direct measurement.

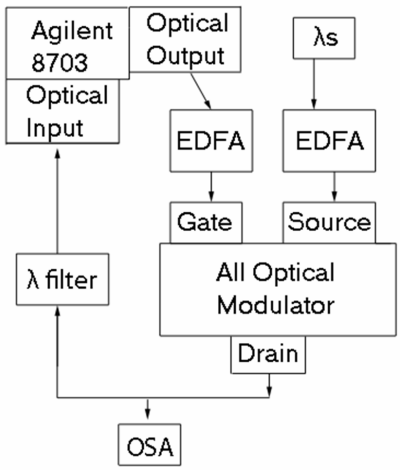

Figure 7.8: Logical diagram of setup used for amplitude modulation measurement.

In this experiment, a single laser was used as the gate signal. This laser was amplitude modulated and then fed through an EDFA and into the device under test. The signal wavelength path was identical to that in the previously described experiment.

Detection was performed by feeding the output at the drain port through a wavelength filter (to remove the source wavelength) and then into a diode photodetector. Both the modulator and photodetector were integrated into the vector network analyzer, which is specifically designed and calibrated for a lightwave component test. The gate power was set up to be 17 dBm at the modulation arm, and the source power 10 dBm.

Briefly, when used in the optical domain, the Agilent 8703 measures an optical "S-parameter," which is essentially the measurement of the ability of a device to transfer an intensity modulation from one optical signal to another. At the heart of this device is a simple Fourier filter applied to the current output from a 20 GHz turn on time photodiode. Significantly, one would not expect such a measuring device to notice the phase of any incoming light, in contrast to the OSA. Only the intensity can be seen.

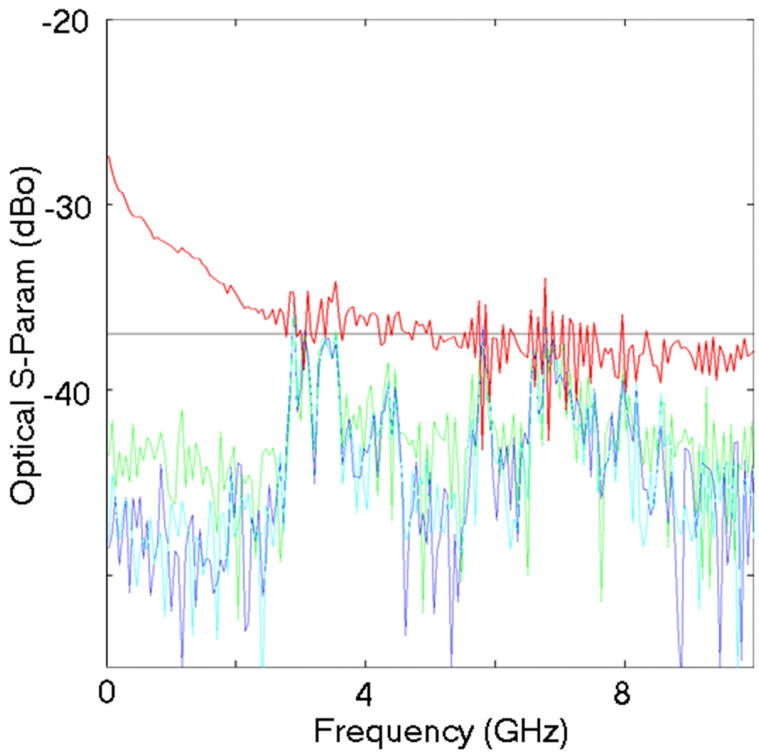

Figure 7.9: Optical S-parameter due to intensity modulation detector. The red curve is the measured value of the S-parameter when both the gate and source lasers are on. For

control, we show the same measurement taken when the signal laser is off, when the pump is off, and when all lasers are off, shown with the green, blue, and teal curves, respectively. The predicted S-parameter from the dual gate experiment is also shown as a black line, and is found to be in close agreement with the S-parameter measured.

Typical output is shown in figure 7.9. The S-parameter between the optical modulation on the gate and that which is received on the source wavelength at the drain port was found to be around -38 dB at 4 GHz. This is in close agreement with the value of the S-parameter that can be calculated based upon the spectral data measured at 2.6 THz, as shown in the figure. This comparison is done through the use of the previously given formula relating the relative extinction to the phase shift seen. This shows that across three orders of magnitude in speed, the response of this modulator is approximately flat.

Bibliography

[1]: B. Saleh, M. Teich, *Fundamentals of Photonics* (Wiley, New York, 1991)

[2]: J. Hecht, *City of Light* (Oxford, New York, 1999)

[3]: W. Koechner, *Solid-State Laser Engineering* (Springer, Berlin, 1999)

[4]: T. Baehr-Jones, M. Hochberg, C. Walker, et al., "High-Q resonators in thin silicon-on-insulator," Applied Physics Letters 85, 3346-3347 (2004).

[5]: Luxtera, Inc., *Fiber will displace copper sooner than you think* (www.luxtera.com, 2005)

[6]: T. Baehr-Jones, M. Hochberg, A. Scherer, "A distributed implementation of the finite-difference time domain (FDTD) method", Applied Computational Electromagnetics Society, 2001 Symposium Proceedings of ACES (Monterey, CA): 671-675.

[7]: J. Jackson, *Classical Electrodynamics* (Wiley, New York,. 1998)

[8]: A. Watt, *3D Computer Graphics* (Addison-Wesley, Harlow, 1993)

[9]: A. Taflove, *Comutational Electrodynamics,* (Artech House, Boston, 1995)

[10]: K. Eriksson, D. Estep, P. Hansbo, C. Johnson, *Computational Differential Equations* (Cambridge University Press, Cambridge, 1996)

[11]: K. Okamoto, *Fundamentals of Optical Waveguides* (Academic Press, San Diego, 2000)

[12]: M. Hochberg, T. Baehr-Jones, C. Walker, et al., "Segmented waveguides in thin silicon-on-insulator," Journal of the Optical Society of America B 22, 1493-1497 (2005).

[13]: J. Joannopoulos, R. Meade, J. Winn, *Photonic Crystals* (Princeton University Press, Princeton, 1995)

[14]: T. Baehr-Jones, "Simulation and characterization of a ring resonator," Senior Thesis, Caltech, 2002.

[15]: T. Baehr-Jones, M. Hochberg, C. Walker, and A. Scherer, "Analysis of the tuning sensitivity of silicon-on-insulator optical ring resonators," IEEE J. Lightwave Technology 23, 4215-4221 (2005).

[16]: B. Streetman, *Solid State Electronic Devices* (Prentice Hall, 2005).

[17]: International Technology Roadmap for Semiconductors (public.itrs.net/, 2006).

[18]: M. Borselli, T. Johnson, O. Painter, "Beyond the rayleigh scattering limit in high-Q silicon microdisks: theory and experiment," Optics Express 13, 1515-1530 (2005).

[19]: "Pacific wave unveils modulator," Light Reading, June 8, 2001.

[20]: V. Almeida, R. Panepucci, M. Lipson, "Nanotaper for compact mode convesion," Optics Letters 28, 1302-1304, 2003.

[21]: D. Taillaert, W. Bogaerts, P. Bienstman, et al. "An out-of-plane grating coupler for efficient butt-coupling between compact planar waveguides and single-mode fibers," IEEE Journal of Quantum Electronics 38, 949-955, 2002.

[22]: A. Yariv, " Critical coupling and its control in optical waveguide-ring resonator systems," IEEE Photonics Technology Letters 14, 483-485, 2002.

[23]: M. Hochberg, T. Baehr-Jones, C. Walker, et al., "Segmented waveguides in thin silicon-on-insulator," Journal of the Optical Society of America B 22, 1493-1497 (2005).

[24]: C. Kittel, *Introduction to Solid State Physics* (Wiley, New York, 1996)

[25]: T. Nikolajsen, K. Leosson, I. Salakhutdinov, and S. Bozhevolnyi, “Polymer-based surface-plasmon-polariton stripe waveguides at telecommunication wavelengths,” Applied Phyics. Letters *82*, 668-670 (2003).

[26]: J. Takahara, Y. Suguru, T. Hiroaki, A. Morimoto, and T. Kobayashi, “Guiding of a one-dimensional optical beam with nanometer diameter,” Optics Letters 22, 475-477 (1997).

[27]: J. Vuckovic, M. Loncar, and A. Scherer, “Surface plasmon enhanced light-emitting diode,” IEEE J. Quantum Electron. 36, 1131-1144 (2000).

[28]: S. A. Maier, P. G. Kik, H. A. Atwater, S. Meltzer, E. Harel, E. E. Koel, and A. A. Requicha, “Local detection of electromagnetic energy transport below the diffraction limit in metal nanoparticle plasmon waveguides,” Nature Materials 2, 229-232 (2003).

[29]: W. Henschel, Y. M. Geirgiev, and H. Kurz, “Study of a high contrast process for hydrogen slisesquioxane as a negative tone electron beam resist,” Journal of Vacuum Science & Technology B: Microelectronics and Nanometer Structures 21, 2018-2025 (2003).

[30]: I. W. Rangelow, and H. Loschner, “Reactive ion etching for microelectrical mechanical system fabrication,” Journal of Vacuum Science & Technology B: Microelectronics and Nanometer Structures 13, 2394-2399 (1995).

[31]: G. Reed, “The Optical age of Silicon”, Nature 427 (2004).

[32]: C. Zhang, L. R. Dalton, M. C. Oh, H. Zhang, W. H. Steier, “ Low V-pi electrooptic modulators from CLD-1: Chromophore design and synthesis, material processing, and characterization,” Chem. Mater. **13**, 3043-3050 (2001).

[34]: Q. Xu, V. Almeida, C. Barrios, R. Panepucci, M. Lipson, "Silicon void nano-waveguides for guiding and confining light," 2004 Conference on Lasers and Electro-Optics (CLEO), Vol. 2, p. 107-109, 16-21 May 2004.

[35]: T. Baehr-Jones, M. Hochberg, C. Walker, et al., "High-Q optical resonators in Silicon-On-Insulator based slot waveguides," Applied Physics Letters 86, Art. No. 081101 (2005).

[36]: H. Ma, S. Liu, S. Suresh, L. Liu, S. Kang, M. Haller, T. Sassa, L. Dalton, A. Jen, "Highly efficient and thermally stable electro-optical dendrimers for photonics," Advanced Functional Materials 12, 565-574 (2002).

[37]: T. Kim, JD. Juo, JW. Kang, M. Haller, Y. Tian, L. Dalton, A. Jen, **"**Molecular engineering of highly efficient and thermally stable nonlinear optical polymers for electro-optics," Abstracts of Papers of the American Chemical Society 228, U438-U438 (2004).

[38]: S. Miyata, H. Sasabe, *Poled Polymers and their Applications to SHG and EO device* (Gordon and Breach Science Publishers, Australia, 1997).

[40]: S. Graf, H. Sigg, W. Bachtold, "High-frequency electrical pulse generation using optical rectification in bulk GaAs," Appl. Phys. Lett. 76**,** 2647-2649 (2000).

[41]: R. Boyd, *Nonlinear Optics* (Elsevier Science, San Diego, 2003)

[42]: T. Londergan, C. Zhang, A. Ren, L. Dalton, "Dendrimer-functionalized NLO chromophores," Abstracts of Papers of the American Chemical Society 219, U410-U410 366-POLY Part 2 (2000).

[43]: G. He, S. Liu, *Physics of Nonlinear Optics* (World Scientific, Singapore, 1999)